Eidgenössische
Technische Hochschule
Zürich

Ecole polytechnique fédérale de Zurich
Politecnico federale di Zurigo
Swiss Federal Institute of Technology Zurich

Hybrid FEM/BEM modeling of finite-sized photonic crystals for semiconductor laser beams

M. Durán*, M. Guarini* and C.F. Jerez-Hanckes

Research Report No. 2009-25
August 2009

Seminar für Angewandte Mathematik
Eidgenössische Technische Hochschule
CH-8092 Zürich
Switzerland

*Pontificia Universidad Católica de Chile, Facultad de Ingeniería, Av. Vicuña Mackenna 4860, Santiago, Chile

Hybrid FEM/BEM modeling of finite-sized photonic crystals for semiconductor laser beams.

M. Durán[†], M. Guarini[†] and C. F. Jerez-Hanckes[*,‡]

Abstract

We propose a 2-D finite-element/boundary-element hybrid method for calculating the spatial distribution and frequency response of electromagnetic waves coming from a semiconductor laser when interacting with a finite-sized photonic crystal. We thus provide a flexible tool for the design of novel optical and microwave devices, among other applications. In opposition to current methodologies, we simultaneously take into account the laser modes, the finiteness of the crystal, and the unboundedness of the isotropic medium in which the crystal is embedded. At the laser output, instead of approximating reflected and transmitted beams by plane waves, we use the more realistic Hermite-Gauss functions. In the isotropic medium, we set an artificial boundary encircling the crystal and define exterior and interior domains. Radiating solutions for the scattered far-field over the exterior are derived analytically through a series of Hankel polynomials. The interior domain is described by a finite-element formulation coupled with Dirichlet-to-Neumann maps enforcing laser and far-field behaviors. Results and error analyses are provided in view of future improvements.

1 Introduction

Since the work by Yablonovitch [1], tremendous interest has been set towards the investigation and design of so-called Photonic Crystals (PCs) [2, 3]. These are a novel type of material in which the refractive index varies periodically with position. The resulting Bragg scattering of electromagnetic waves leads to the formation of a band structure which is, in several ways, analogous to the band structure in semiconductors. Under suitable design of lattice symmetry and refraction index contrasts, PCs may exhibit complete photonic bandgaps (PBGs), i.e., ranges of frequencies over which ordinary (linear) propagation is forbidden, irrespective of the propagation direction. By introducing defects in the lattice, specific frequencies can be selected inside the bandgap and light paths can be designed. Hence, the engineering of these materials offers enormous potential for applications ranging from basic science like localization of light [4] to optical telecommunication devices such as demultiplexers [5] or add-drop filters [6]. In particular, we will concentrate on their use as filters for semiconductor lasers, a cornerstone of modern technology.

[*]ETH Zürich, Seminar für Angewandte Mathematik, Zürich, Switzerland
[†] Pontificia Universidad Católica de Chile, Facultad de Ingeniería, Santiago, Chile
[‡] Correspondence to: C. F. Jerez-Hanckes. Email: cjerez@sam.math.ethz.ch

Along with their advantages in power consumption and versatility, semiconductor lasers have certain drawbacks in regard to their spectrum definition and field profile [16, 17]. In the case of the ubiquitous double heterojunction (DH) stripe geometry injection lasers, the generated field profiles are astigmatic and highly elliptical [18], requiring correction by external and often costly structures. Furthermore, most semiconductor lasers allow multimode oscillation [19, 20]. This is due to the large spectral width of the gain coefficient which, regardless of the small resonator length, still allows several modes to resonate. Such multimode operation is also undesirable and different means have been designed to ameliorate this [21].

Clearly, photonic crystals can address the laser's frequency problem if adequately tailored. That they can concurrently collimate beams is less known. Indeed, subwavelength light focusing by PCs has been recently observed both experimentally and numerically through finite-difference time-domain (FDTD) simulations [22, 23]. Under particular conditions, light passing through the PC focuses on a size smaller than a wavelength in contradiction to the diffraction limit principle. This occurs when the photonic band diagram possesses a convex topology and negative refraction takes place [24]. In the experiments performed by Kramper *et al.* [23], they show that it is possible to couple out directional beams from PC waveguides if they are terminated properly, i.e., when the PC-air interface is such that surface modes are excited. This observation provides a way to counteract the wide-angle beam for the DH laser and motivates the present work. Nonetheless, other applications include the design of highly directional antennae from omnidirectional sources as proposed by Ozbay *et al.* [24].

Grounded on these physical arguments, we aim to provide a suitable numerical scheme for designing spatial and frequency filters based on PC structures for a semiconductor laser (see Figure 1). Therefore, we need to simultaneously describe the following aspects:

- reflection and transmission of actual lasing modes;
- wave diffraction caused by a finite photonic crystal slab – structures with a finite number of identical cells; and,
- outgoing nature of scattered radiation as it propagates away from the crystal over the infinite isotropic medium.

Now, the modeling of PCs from first principles or *ab initio* is encouraged by the close agreement between simulation and experiment. Furthermore, the scalability of Maxwell's equations enables a given design to be used in any frequence range – although we will be mostly interested in infrared and optical wavelengths. Hence, numerous models and solution techniques have been developed [7]. Altogether, several issues remain untackled and constitute challenging problems. In this work, we address the analysis of radiation losses in optically integrated circuits [8, 9]; and, in a lesser extent, the distorsion of PBGs due to the finiteness of the crystal [10].

Due to the geometric complexity of the structures devised, most modeling approaches assume a periodic array or infinite crystal whose band diagram is obtained by the conventional plane-wave method [11]. In the recent work by Wu *et al.* [15], this technique is extended to describe finite-crystals by using an

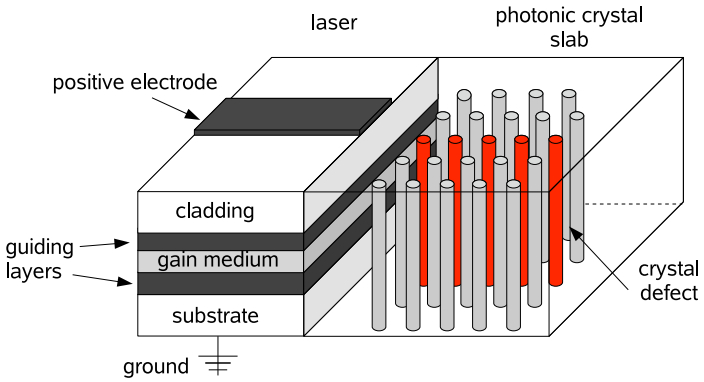

Figure 1: 3-D diagram portraying an heterojunction laser facing a photonic crystal slab. The 2-D model is taken at the center plane of the gain layer wherein photon generation takes place via electron-hole recombination after applying a certain voltage. Dimensions are not in scale.

effective propagation constant and a frequency-dependent dielectric constant. Nonetheless, it still assumes plane-wave functions which may not represent the actual beam profile, that is, the one coming from lasers. Finite-sized structures have also been modeled via FDTD using absorbing boundary conditions, and by applying the finite-element method (FEM) enhanced with perfectly matched layers (PML) [12, 13]. Unfortunately, these techniques do not automatically yield the actual far-field radiation profiles requiring post-treatment. Moreover, FDTD methods are well-known to be unstable when accounting for fine features and can provide spurious modes [14].

In this article, we consider the system described in Figure 1 and neglect the vertical direction as a first step towards the full $\mathbb{R}^3$-representation. The associated 2-D model is set along the plane corresponding to that of crystal periodicity and the gain medium. We propose to artificially divide the photonic slab into exterior and interior domains. Outside the fictitious boundary, solutions are found as a particular series of Hankel polynomials which account for radiation conditions at infinity. Description of the lasing system at the input interface is achieved by an eigenfunction expansion of Hermite-Gauss (HG) functions that yields the accurate behavior of the laser. On the interior domain, fields are calculated using finite elements which easily take care of refraction index variations. Coupling between laser and outgoing wave behaviors is attained by transmission conditions enforced by Dirichlet-to-Neumann (DtNs) maps over the common boundaries. This calls for variants of the boundary element method (BEM), and their agreement with the finite-element approximation coming from the interior domain.

Combinations of the FEM and BEM have been extensively studied in many settings as can be seen in [25, 26, 27, 28, 29, 30], among many other works. The idea behind all of them is to derive accurate solutions by mixing the flexibility of the FEM to model complex structures with the efficiency of the BEM to condense information at the boundaries and eventually describe unbounded media. In our case, the originality of the proposed approach is to combine the behavior

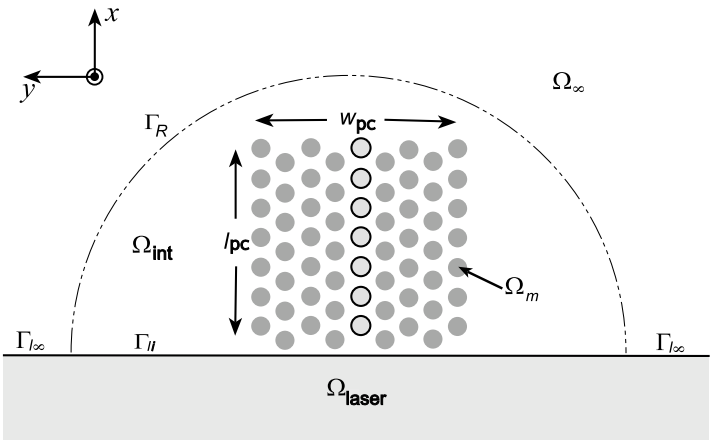

Figure 2: Coordinate and subdomain definitions. Coordinate axes are centered at the laser/crystal interface Γ_l and the middle of the crystal. Note the splitting of the interface boundary Γ_l into $\Gamma_{l\infty}$ and Γ_{li} induced by the artificial domain decomposition Ω_{int} and Ω_∞.

coming from the laser itself and adapt the far-field eigenmodes of the exterior solution to deliver a FEM/BEM formulation which tries to efficiently portray as much of the real physics as possible. The role of the finite-element modeled domain is to combine these two behaviors and describe the complex near-field scattering provoked by the PC. Consequently, the key feature of our model is the extensive use of *a priori* information to represent the system in a physically realistic way in affordable computational times. Moreover, the proposed methodology can be used for a larger range of applications and modifications can be easily made to account for more complex phenomena.

This paper is structured as follows. In Section 2, we define the geometrical characteristics, physical quantities and mathematical setting of the proposed 2-D model. Eigenfunction expansions for imposing boundary conditions are presented in Section 3. Therein, the division of the original problem into two dependent ones is presented as well as the variational formulation involved. In Section 4, domain and solution discretizations are described along with boundary elements employed. More details regarding approximation schemes are given in the Appendices. In Section 5, physical parameters are further specified and simulation results are analyzed and discussed. Finally, conclusions and future developments are drawn in Section 6.

2 Model Description

2.1 Geometry

We are interested in analyzing the transmission properties of the output beam of a double heterojunction semiconductor laser immediately scattered by a finite 2-D photonic crystal slab, as shown in Figure 1. We neglect vertical variations and consider exclusively the plane given by that of PC periodicity and laser gain layer. Figure 2 depicts the choice of coordinates $\mathbf{x} = (x, y)$ describing this

plane with directions given by unitary vectors $\mathbf{e}_x$ and $\mathbf{e}_y$.

We assume the direction of laser propagation to be along $\mathbf{e}_x$ (positive x-axis). The laser is located at the lower half-plane denoted by Ω_{laser} and the PC is placed on the exterior domain, Ω, i.e.,

$$\text{laser domain} \qquad \Omega_{\text{laser}} := \left\{(x,y) \in \mathbb{R}^2 \,:\, x < 0\right\}, \tag{1a}$$

$$\text{exterior of laser domain} \qquad \Omega := \left\{(x,y) \in \mathbb{R}^2 \,:\, x > 0\right\}, \tag{1b}$$

$$\text{laser output} \qquad \Gamma_l := \left\{(x,y) \in \mathbb{R}^2 \,:\, x = 0\right\}, \tag{1c}$$

satisfying $\Omega_{\text{laser}} \cap \Omega = \emptyset$ and $\mathbb{R}^2 = \bar{\Omega}_{\text{laser}} \cup \bar{\Omega}$. A finite 2-D lattice of width w_{pc} and length l_{pc}, containing M circles, with bounded $M \in \mathbb{N}_0$, represents the two-dimensional PC structure. These circles or *inclusions*, denoted by $\{\Omega_m\}_{m=1}^{M} \subset \Omega$, are mutually disjoint, have radii $\{a_m\}_{m=1}^{M}$, and are centered at hexagonally symmetric positions $\{\mathbf{c}_m\}_{m=1}^{M}$, such that, for each m, we set

$$m\text{-th inclusion} \qquad \Omega_m := \left\{\, \mathbf{x} \in \Omega \,:\, \|\mathbf{x} - \mathbf{c}_m\| < a_m \right\}, \tag{2a}$$

$$m\text{-th inclusion boundary} \qquad \partial\Omega_m := \left\{\, \mathbf{x} \in \Omega \,:\, \|\mathbf{x} - \mathbf{c}_m\| = a_m \right\}, \tag{2b}$$

where $\|\cdot\|$ is the classic euclidean norm. The choice of hexagonal periodicity is explained in Section 5.1. Define the integer set identifying all inclusions by $\mathfrak{M} = \{1, \ldots, M\}$, wherein those corresponding to defects in the crystal are indicated by a subset of indices $\mathfrak{D} \subsetneq \mathfrak{M}$ of smaller cardinality, $D \in \mathbb{N}_0$, i.e., $D < M$. The physical and geometrical properties of defect inclusions can eventually differ from the rest. In fact, the inclusions defining the *base crystal* are the majority sharing the same geometrical and physical properties, as for instance $a_m = a$ for all $m \in \mathfrak{M} \setminus \mathfrak{D}$ with values of a established later on. We can define the subdomains:

$$\text{photonic crystal} \qquad \Omega_{\text{pc}} := \bigcup_{m \in \mathfrak{M}} \Omega_m, \tag{3a}$$

$$\text{crystal defect} \qquad \Omega_{\text{def}} := \bigcup_{m \in \mathfrak{D}} \Omega_m \subsetneq \Omega_{\text{pc}}, \tag{3b}$$

$$\text{connected subdomain in } \Omega \qquad \Omega_{\text{con}} := \Omega \setminus \bar{\Omega}_{\text{pc}}, \tag{3c}$$

$$\text{photonic crystal boundary} \qquad \partial\Omega_{\text{pc}} := \bigcup_{m \in \mathfrak{M}} \partial\Omega_m. \tag{3d}$$

Set $R \in \mathbb{R}$ positive and bounded. For computational reasons, Ω is further divided into two subdomains:

$$\Omega_{\text{int}} := \{\mathbf{x} \in \Omega \,:\, \|\mathbf{x}\| < R\} \qquad \text{and} \qquad \Omega_{\infty} := \Omega \setminus \bar{\Omega}_{\text{int}} \tag{4}$$

where Ω_{int} is bounded and contains the photonic crystal Ω_{pc}. If $\partial\Omega_{\text{int}}$ denotes the boundary of Ω_{int}, this splitting introduces an artificial boundary, Γ_R, given by a half-circumference centered at the origin with radius R, i.e., $\Gamma_R := \Omega \cap \partial\Omega_{\text{int}}$. The remaining relevant domains and boundaries are

$$\text{connected subdomain in } \Omega_{\text{int}} \qquad \Omega_{\text{sub}} := \Omega_{\text{int}} \cap \Omega_{\text{con}}, \tag{5a}$$

$$\text{boundary of } \Omega_{\text{sub}} \qquad \partial\Omega_{\text{sub}} := \partial\Omega_{\text{int}} \cup \partial\Omega_{\text{pc}}, \tag{5b}$$

$$\text{laser output in } \bar{\Omega}_i \qquad \Gamma_{li} := \left\{\, \mathbf{x} \in \Gamma_l \,:\, \|\mathbf{x}\| < R \right\}, \tag{5c}$$

$$\text{laser output in } \bar{\Omega}_{\infty} \qquad \Gamma_{l\infty} := \Gamma_l \setminus \bar{\Gamma}_{li}, \tag{5d}$$

and consequently, the boundary $\partial\Omega_{\text{int}}$ is equal to $\Gamma_R \cup \bar{\Gamma}_{li}$. These definitions are shown in Figure 2.

With this picture in mind, the physics of our problem can be easily described when in steady-state operation. An incoming laser beam comes directly from Ω_{laser}, following $\mathbf{e}_x$, with a profile known in advance. Depending upon the properties of the lattice, part of the scattered radiation will return to the device as a linear combination of the allowed laser modes. The remaining radiation propagates over Ω_{int} crossing Γ_R and continues at infinity in Ω_∞. This radiation contains scattered terms that must decay at infinity even though the terms associated to the incoming wave do not. Nonetheless, both waves are ruled by the Helmholtz equation as shown below.

2.2 Maxwell's equations. TM and TE decompositions

We assume the solutions over Ω_{laser} of the unperturbed lasing problem to be known (see Section 3.1). Thus, we focus on solving the electromagnetic fields on the entire half-plane Ω and start by recalling a few concepts before arriving at the exact formulation. The set of harmonic Maxwell's equations that governs light in the absence of free charges and currents is [31]

$$\nabla \times \mathbf{E} = \imath\,\omega\,\mu_o \mathbf{H} \tag{6a}$$

$$\nabla \times \mathbf{H} = -\imath\,\omega\,\epsilon_o\,\epsilon(\mathbf{x})\mathbf{E} \tag{6b}$$

$$\nabla \cdot \mathbf{H} = 0 \tag{6c}$$

$$\nabla \cdot \epsilon_o\,\epsilon(\mathbf{x})\mathbf{E} = 0 \tag{6d}$$

with $\mathbf{E}$ and $\mathbf{H}$ being the electric and magnetic vector-fields in $\mathbb{R}^3$, respectively. We utilize the time convention $\exp(-\imath\omega t)$ and the following linear constitutive relations:

$$\mathbf{D} = \tilde{\epsilon}(\mathbf{x})\mathbf{E} \qquad \text{with} \qquad \tilde{\epsilon}(\mathbf{x}) = \epsilon_o\,\epsilon(\mathbf{x})\,, \tag{7a}$$

$$\mathbf{B} = \tilde{\mu}\mathbf{H} \qquad \text{with} \qquad \tilde{\mu} = \mu_o\,\mu\,. \tag{7b}$$

The dependence of the dielectric constant on position is made explicit by defining $\tilde{\epsilon}(\mathbf{x})$ as the product between the dielectric coefficient at vacuum, ϵ_o, and the relative dielectric constant, $\epsilon(\mathbf{x})$, a dimensionless parameter. If constant values are assigned over each subdomain, one can construct a relative dielectric coefficient defined over Ω, $\epsilon(\mathbf{x}) \in L^\infty(\Omega)$, as follows:

$$\epsilon(\mathbf{x}) = \begin{cases} \epsilon_{\text{def}} & \text{if} \quad \mathbf{x} \in \Omega_{\text{def}}\,, \\ \epsilon_{\text{base}} & \text{if} \quad \mathbf{x} \in \Omega_{\text{pc}} \setminus \Omega_{\text{def}}\,, \\ \epsilon_{\text{con}} & \text{if} \quad \mathbf{x} \in \Omega_{\text{con}} \end{cases} \tag{8}$$

where ϵ_{base}, ϵ_{def} and ϵ_{con} are positive and bounded scalars representing the relative dielectric constants for the base crystal, the possible defect inclusions and the unbounded connected media, respectively. Moreover, we denote by ϵ_{laser} the effective permittivity coefficient over Ω_{laser}. Materials are assumed non-magnetic, i.e., $\mu \equiv 1$, so that $\tilde{\mu} = \mu_o$.

Recalling that $c = 1/\sqrt{\epsilon_o\,\mu_o}$ is the speed of light at vacuum and defining the free-space wave number $k_0 = \omega/c$, we obtain two equivalent formulations

over Ω:

$$E\text{-formulation} \quad \begin{cases} \frac{1}{\epsilon(\mathbf{x})}\nabla\times\nabla\times\mathbf{E} \;=\; k_0^2\mathbf{E} \\ \nabla\cdot\epsilon(\mathbf{x})\mathbf{E} \;=\; 0 \end{cases}, \tag{9a}$$

$$H\text{-formulation} \quad \begin{cases} \nabla\times\frac{1}{\epsilon(\mathbf{x})}\nabla\times\mathbf{H} \;=\; k_0^2\mathbf{H} \\ \nabla\cdot\mathbf{H} \;=\; 0 \end{cases}. \tag{9b}$$

Traditionally, Equation (9b) is treated first for solving $\mathbf{H}$ and then obtain $\mathbf{E}$ from (6b). However, when the problem is taken to be two-dimensional (vertical invariance), it can be formulated as two independent scalar ones, according to the polarization of the fields. The found solutions are linearly combined to derive a complete description of the beam. For *transverse electric* (TE) polarization or H_z-polarization we have:

$$\nabla\cdot\left(\frac{1}{\epsilon(\mathbf{x})}\nabla H_z(\mathbf{x})\right) \;=\; -k_0^2 H_z(\mathbf{x}) \tag{10}$$

whereas for the *transverse magnetic* (TM) or E_z-polarized case, it holds

$$\frac{1}{\epsilon(\mathbf{x})}\nabla\cdot(\nabla E_z(\mathbf{x})) \;=\; -k_0^2 E_z(\mathbf{x})\,. \tag{11}$$

The latter can be directly rewritten as:

$$\Delta U(\mathbf{x}) \;+\; k_0^2\epsilon(\mathbf{x})\,U(\mathbf{x}) \;=\; 0 \qquad \text{for} \quad \mathbf{x}\in\Omega\,, \tag{12}$$

where the simplification $U = E_z$ has been made. In the TE case, we take $U = H_z$ and obtain

$$\nabla\cdot\frac{1}{\epsilon(\mathbf{x})}\,\nabla U(\mathbf{x}) \;+\; k_0^2\,U(\mathbf{x}) \;=\; 0 \qquad \text{for} \quad \mathbf{x}\in\Omega\,. \tag{13}$$

Hence, we consider in general the Helmholtz-type equation:

$$\nabla\cdot a(\mathbf{x})\,\nabla U(\mathbf{x}) \;+\; k_0^2\,b(\mathbf{x})\,U(\mathbf{x}) \;=\; 0 \qquad \text{for} \quad \mathbf{x}\in\Omega\,, \tag{14}$$

with polarization-dependent coefficients:

$$\text{TM} \quad \begin{cases} a(\mathbf{x}) \;\equiv\; 1 & \mathbf{x}\in\Omega \\ b(\mathbf{x}) \;\equiv\; \epsilon(\mathbf{x}) & \mathbf{x}\in\Omega \end{cases}, \quad \text{TE} \quad \begin{cases} a(\mathbf{x}) \;\equiv\; \epsilon^{-1}(\mathbf{x}) & \mathbf{x}\in\Omega \\ b(\mathbf{x}) \;\equiv\; 1 & \mathbf{x}\in\Omega \end{cases}. \tag{15}$$

This supports the choice of variational forms for finding solutions, as required for the finite element method (see Section 3.4). An alternative approach consists in exclusively using the classical Helmholtz equation (12) over each of the subdomains. Since the permittivity is piecewise constant, in (13) $\nabla\epsilon^{-1}$ is different from zero only when passing through the interior boundaries. Thus, in a variational formulation, the gradient of ϵ^{-1} becomes a boundary integral which requires to be imposed explicitly. This, however, demands an extra effort as boundary elements need to be defined over each subdomain boundary.

2.3 TE and TM transmission conditions

Keeping U for writing normal field components in Ω, let us introduce the shorthand:

$$U_\alpha \;:=\; U|_{\Omega_\alpha} \;=\; \{\, U(\mathbf{x}) \,:\, \mathbf{x} \in \Omega_\alpha \} \;, \tag{16}$$

denoting field values over any of the subdomains Ω_α previously defined (see Figure 3). We assume normal vectors $\mathbf{n}_\alpha$ to point outwards each subdomain boundary $\partial\Omega_\alpha$ with unitary norm. Hence, at the interface between two contiguous domains Ω_α and Ω_β, the normals will have the same direction but opposite senses, i.e.,

$$\mathbf{n}_\alpha\big|_{\partial\Omega_\alpha \cap\, \partial\Omega_\beta} \;=\; -\mathbf{n}_\beta\big|_{\partial\Omega_\alpha \cap\, \partial\Omega_\beta} \;. \tag{17}$$

For TE polarization, the Neumann transmission condition for adjacents domains is given by normal continuity of the displacement vectors:

$$\frac{1}{\epsilon_\alpha}\frac{\partial U_\alpha}{\partial n}\bigg|_{\partial\Omega_\alpha} \;=\; -\frac{1}{\epsilon_\beta}\frac{\partial U_\beta}{\partial n}\bigg|_{\partial\Omega_\beta} \qquad \text{TE Neumann,} \tag{18}$$

while for TM waves, one has

$$\frac{\partial U_\alpha}{\partial n}\bigg|_{\partial\Omega_\alpha} \;=\; -\frac{\partial U_\beta}{\partial n}\bigg|_{\partial\Omega_\beta} \qquad \text{TM Neumann.} \tag{19}$$

Continuity of normal field components across the interfaces for both polarizations, yields Dirichlet transmission conditions:

$$U_\alpha\big|_{\partial\Omega_\alpha} \;=\; U_\beta\big|_{\partial\Omega_\beta} \qquad \text{Dirichlet.} \tag{20}$$

2.4 Scattered and incident parts field decomposition

By linearity of the physical system, one can split the fields into

$$U \;=\; U^{\text{inc}} \,+\, U^{\text{sc}} \tag{21}$$

where U^{sc} is the scattered part and U^{inc} is the incoming field, a known solution for Equation (12) in an isotropic medium. Hence, for each subdomain Ω_α defined in Section 2.1, we introduce the restrictions:

$$U^{\text{inc}}_\alpha \;:=\; U^{\text{inc}}\big|_{\Omega_\alpha} \qquad \text{and} \qquad U^{\text{sc}}_\alpha \;:=\; U^{\text{sc}}\big|_{\Omega_\alpha} \;, \tag{22}$$

implying

$$U_\alpha \;=\; U^{\text{inc}}_\alpha \,+\, U^{\text{sc}}_\alpha \;. \tag{23}$$

Notice also that this decomposition can be extended to trace quantities as employed below.

2.5 Problem formulation at Ω

Let $H^1_{\text{loc}}(\Omega)$ be the Sobolev space of functions which along with their first-order derivatives are locally square-integrable on Ω. Its associated trace spaces are $H^{1/2}(\Gamma_l)$ and $H^{-1/2}(\Gamma_l)$ [32]. Later on, we will also work in the space of functions that can be extended by zero, which are differentiated by adding a tilde, e.g., $\widetilde{H}^{1/2}(\Gamma_l)$.

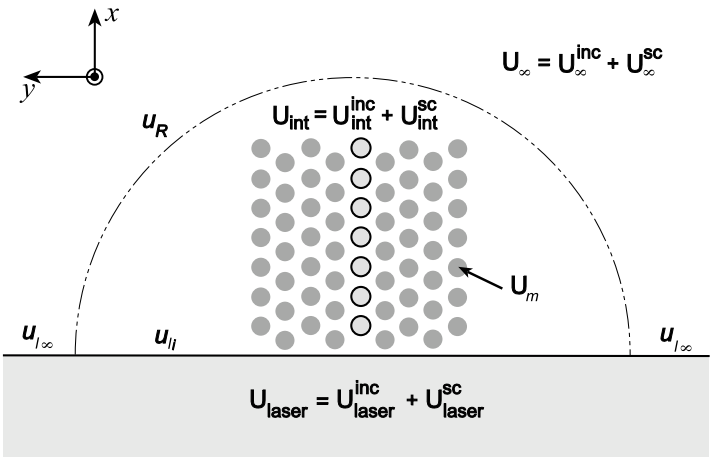

Figure 3: Notation for field restrictions over subdomains and their decomposition into incident and scattered terms. Trace values are written in lower case.

Define U_{laser} as the solution over Ω_{laser}. Then, the strong form of the problem in Ω for both polarizations can be posed as follows: seek $U \in H^1_{\text{loc}}(\Omega)$ such that

$$(P_o)\begin{cases} \nabla \cdot a(\mathbf{x})\,\nabla U(\mathbf{x}) \;+\; k_0^2\, b(\mathbf{x})\, U(\mathbf{x}) \;=\; 0 & \text{for } \mathbf{x} \text{ in } \Omega\,, \\ +\,\text{coupling conditions with } U_{\text{laser}} & \text{on } \Gamma_l\,, \\ +\,\text{radiation conditions for the scattered field} & \|\mathbf{x}\| \longrightarrow \infty\,, \quad \mathbf{x} \in \Omega\,. \end{cases} \tag{24}$$

Well-posedness of the above problem can be achieved by establishing the Dirichlet-to-Neumann maps coupling U and U_{laser} over Γ_l (see Section 3.1). This is related to the continuity of both Dirichlet- and Neumann-type traces. From (20), it holds

$$U\big|_{\Gamma_l} \;=\; U_{\text{laser}}\big|_{\Gamma_l} \;=:\; u_l \;\in\; H^{1/2}(\Gamma_l) \tag{25}$$

where we have defined the trace over Γ_l, u_l, as a new unknown. In the following, we write boundary quantities in lower case to distinguish them from values over subdomains given in capital letters. From Section 2.3, Neumann traces at the laser interface Γ_l must satisfy either

$$\text{TE}: \quad \frac{1}{\epsilon_{\text{laser}}}\frac{\partial U_{\text{laser}}}{\partial x}\bigg|_{\Gamma_l} \;=\; \frac{1}{\epsilon}\frac{\partial U}{\partial x}\bigg|_{\Gamma_l} \qquad \text{or} \qquad \text{TM}: \quad \frac{\partial U_{\text{laser}}}{\partial x}\bigg|_{\Gamma_l} \;=\; \frac{\partial U}{\partial x}\bigg|_{\Gamma_l}\,, \tag{26}$$

where $\mathbf{n}$ is in fact heading towards $\mathbf{e}_x$. Moreover, the above traces lie in $H^{-1/2}(\Gamma_l)$.

2.6 Problem formulations over Ω_{int} and Ω_∞

As it stands, the above problem is not suitable for a numerical scheme as both the domain Ω and the boundary Γ_l are unbounded. To handle this, we divide the original problem over Ω, (P_o), into two coupled ones:

1. (P_{int}) defined over Ω_{int}, wherein a solution denoted U_{int} is computed through the FEM; and,

2. (P_∞) whose solution, U_∞^{sc}, is the scattered field over Ω_∞, obtained as a linear combination of eigenfunctions of the isotropic half-plane.

The link between both problems is achieved via continuity conditions for the Dirichlet and Neumann traces at Γ_R. The Dirichlet transmission condition for the total field reads

$$U_\infty\big|_{\Gamma_R} \;=\; U_{\text{int}}\big|_{\Gamma_R} \;=:\; u_R \;\in\; H^{1/2}(\Gamma_R)\;, \tag{27}$$

and hence, the defined trace u_R constitutes another boundary unknown besides u_l. For the moment, we can neglect U^{inc} as it is known everywhere and write the conditions only for the scattered parts. Specifically, it must hold

$$U_\infty^{\text{sc}}\big|_{\Gamma_R} \;=\; U_{\text{int}}^{\text{sc}}\big|_{\Gamma_R} \;=:\; \varphi_R \;\in\; H^{1/2}(\Gamma_R)\;, \tag{28a}$$

$$\left.\frac{\partial U_\infty^{\text{sc}}}{\partial r}\right|_{\Gamma_R} \;=\; \left.\frac{\partial U_{\text{int}}^{\text{sc}}}{\partial r}\right|_{\Gamma_R} \;=:\; \psi_R \;\in\; H^{-1/2}(\Gamma_R)\;, \tag{28b}$$

where we have defined the trace unknowns φ_R and ψ_R, related to each other by the Dirichlet-to-Neumann operator introduced in Section 3.3. Notice that we have used the exterior normal to Ω_{int} at Γ_R, $\mathbf{n}_{\text{int}} = \mathbf{r}/\left\|\mathbf{r}\right\|$. Moreover, transmission conditions are independent from the polarization due to the artificial character of the boundary.

We must now characterize the coupling between the solution of (P_o) and the one over Ω_{laser} – Equations (25) and (26) – for the artificial splitting (P_{int}) and (P_∞). By definition of u_l, (25), the decomposition of the entire solution U over Ω into scattered and incoming terms allows the next definitions:

$$u_l^{\text{inc}} \;:=\; U^{\text{inc}}\big|_{\Gamma_l} \qquad \text{and} \qquad u_l^{\text{sc}} \;:=\; U^{\text{sc}}\big|_{\Gamma_l}\,. \tag{29}$$

Let us assume the trace of U to be null over $\Gamma_{l\infty}$ so as to simplify (P_∞). Although an approximation, this is not far from reality as laser radiation is focalized and scattered energy decays away from the obstacles. This can be written as

$$U_{\text{laser}}\big|_{\Gamma_{l\infty}} \;=\; U\big|_{\Gamma_{l\infty}} \;=\; U_\infty\big|_{\Gamma_{l\infty}} \;=\; 0 \tag{30}$$

In other words, the sum of the traces of U_∞^{inc} and U_∞^{sc} vanishes over $\Gamma_{l\infty}$. On the other hand, the incoming wave is also compactly supported in Γ_{li}. This immediately implies $U^{\text{sc}}|_{\Gamma_{l\infty}} \equiv 0$.

Now, recalling that $U_{\text{laser}}^{\text{sc}}$ is the scattered solution in Ω_{laser}, one can write the coupling at Γ_{li} through two new boundary unknowns, φ_{li} and ψ_{li} shown next. Dirichlet continuity establishes

$$U_{\text{laser}}^{\text{sc}}\big|_{\Gamma_{li}} \;=\; U_{\text{int}}^{\text{sc}}\big|_{\Gamma_{li}} \;=:\; \varphi_{li} \;\in\; \widetilde{H}^{1/2}(\Gamma_{li})\;, \tag{31}$$

while for the Neumann one, we define polarization-dependent unknowns ψ_{li}^{TM} and ψ_{li}^{TE}, both in $H^{-1/2}(\Gamma_{li})$, as

$$\left.\frac{\partial U_{\text{laser}}^{\text{sc}}}{\partial x}\right|_{\Gamma_{li}} \;=\; \left.\frac{\partial U^{\text{sc}}}{\partial x}\right|_{\Gamma_{li}} \;=\; \left.\frac{\partial U_{\text{int}}^{\text{sc}}}{\partial x}\right|_{\Gamma_{li}} \;=:\; \psi_{li}^{\text{TM}} \;\in\; H^{-1/2}(\Gamma_{li})\;, \tag{32a}$$

$$\frac{\epsilon}{\epsilon_{\text{laser}}}\left.\frac{\partial U_{\text{laser}}^{\text{sc}}}{\partial x}\right|_{\Gamma_{li}} \;=\; \left.\frac{\partial U^{\text{sc}}}{\partial x}\right|_{\Gamma_{li}} \;=\; \left.\frac{\partial U_{\text{int}}^{\text{sc}}}{\partial x}\right|_{\Gamma_{li}} \;=:\; \psi_{li}^{\text{TE}} \;\in\; H^{-1/2}(\Gamma_{li})\;. \tag{32b}$$

The scattered field returning to Ω_{laser} is assumed to be a combination of laser modes and accordingly, φ_{li} must take such a form, as detailed in the next section.

Along with the above definitions, radiation conditions at infinity are imposed to the scattered field on the unbounded domain Ω_∞ by taking it to be a solution of the following problem. Define the exterior domain permittivity $\epsilon_\infty := \epsilon_{\text{con}}$. Then, for either polarization we seek $U_\infty^{\text{sc}} \in H^1_{\text{loc}}(\Omega_\infty)$ such that:

$$(P_\infty^{\text{sc}}) \begin{cases} \Delta U_\infty^{\text{sc}}(\mathbf{x}) \,+\, k_0^2\, \epsilon_\infty\, U_\infty^{\text{sc}}(\mathbf{x}) \;=\; 0 & \text{for } \mathbf{x} \text{ in } \Omega_\infty\ , \\ U_\infty^{\text{sc}}\big|_{\Gamma_{l\infty}} \;=\; 0 & \text{over } \Gamma_{l\infty}\ , \\ U_\infty^{\text{sc}}\big|_{\Gamma_R} \;=\; \varphi_R & \text{over } \Gamma_R\ , \\ \lim\limits_{r\to\infty} \left| \dfrac{\partial U_\infty^{\text{sc}}}{\partial r} - \imath k_0 \sqrt{\epsilon_\infty}\, U_\infty^{\text{sc}} \right|^2 = 0 & \text{for } \|\mathbf{x}\| \,=\, r\ ,\ \mathbf{x} \,\in\, \Omega_\infty\ , \end{cases} \tag{33}$$

where the last line is Sommerfeld's radiation condition, which imposes a decaying behavior at infinity for outgoing scattered waves. Solutions are obtained in Section 3 and are dependent on the unknown Dirichlet trace φ_R. With the above conditions, we look for the total field $U_{\text{int}} \in H^1(\Omega_{\text{int}})$ satisfying

$$(P_{\text{int}}) \begin{cases} \nabla \cdot a(\mathbf{x}) \nabla U_{\text{int}}(\mathbf{x}) \,+\, k_0^2\, b(\mathbf{x})\, U_{\text{int}}(\mathbf{x}) \;=\; 0 & \text{for } \mathbf{x} \text{ in } \Omega_{\text{int}}\ , \\ \dfrac{\partial U_{\text{int}}}{\partial n}\Big|_{\Gamma_{li}} \;=\; \dfrac{\partial U_{\text{int}}^{\text{inc}}}{\partial n}\Big|_{\Gamma_{li}} \,+\, \psi_{li} & \text{over } \Gamma_{li}\ , \\ \dfrac{\partial U_{\text{int}}}{\partial n}\Big|_{\Gamma_R} \;=\; \dfrac{\partial U_{\text{int}}^{\text{inc}}}{\partial n}\Big|_{\Gamma_R} \,+\, \psi_R & \text{over } \Gamma_R\ , \end{cases} \tag{34}$$

which is coupled to the solutions over Ω_{laser} and Ω_∞ by φ_{li} and φ_R, respectively.

We next find the eigenfunction expansions for the scattered solution over Ω_∞ and Ω_{laser}. At the boundaries φ_R and φ_{li}, these will be imposed upon the interior problem via Dirichlet-to-Neumann operators that yield ψ_R and ψ_{li}. The interior problem will be solved by first developing the variational formulation and then applying the finite element method.

3 Boundary Eigenfunction Expansions and Variational Formulation

3.1 Laser modes

As described in 2.1, the photonic crystal lies in front of the laser's output. For the stripe geometry double heterojunction laser, lateral modes are produced by a gain-guiding mechanism thoroughly studied in [33, 34, 35, 36]. The analytical solutions proposed for the electric field are Hermite-Gauss functions obtained primarily by the effective index method [37]. Since most injection lasers have fields polarized predominantly along y, we limit our discussion to such modes.

Before reaching the output, the p-th transverse-electric laser mode propagates as $\exp(-\imath\omega t + \imath\beta_p x)$, according to the electric and magnetic fields compo-

nents:

$$E_x^p(y,z) \;=\; \frac{\imath}{\beta_p}\frac{\partial \Psi_p}{\partial y}(y,z)\,, \qquad H_x^p(y,z) \;=\; \frac{\imath}{\omega\mu_0}\frac{\partial \Psi_p}{\partial z}(y,z)\,, \tag{35a}$$

$$E_y^p(y,z) \;=\; \Psi_p(y,z)\,, \qquad H_y^p(y,z) \;=\; \frac{1}{\beta_p\omega\mu_0}\frac{\partial^2 \Psi_p}{\partial z \partial y}(y,z)\,, \tag{35b}$$

$$E_z^p(y,z) \;=\; 0\,, \qquad H_z^p(y,z) \;=\; -\frac{1}{\beta_p\omega\mu_0}\frac{\partial^2 \Psi_p}{\partial y^2}(y,z)\,, \tag{35c}$$

where Ψ_p is equal to the fundamental vertical mode [17] times the normalized p-th lateral mode ψ_p. This is given by

$$\Psi_p(y,z) \;:=\; \cos(\kappa_0 z)\psi_p(y)\,, \qquad \text{for} \quad p \,\in\, \mathbb{N}_0\,, \tag{36}$$

wherein κ_0 is the zeroth-mode eigenvalue along z, and

$$\psi_p(y) \;:=\; \sqrt[4]{\frac{\alpha}{2\pi}}\sqrt{\frac{1}{p!}}\,\mathcal{H}_p(y\sqrt{\alpha})e^{-\frac{1}{4}\alpha y^2}\,, \tag{37}$$

where the constant $\alpha = 2k_0 a_l\sqrt{\Upsilon}$, with Υ being confinement factor for the sandwiched active layer – where photon generation takes place –, and a_l the parameter for parabolic variation in gain index. Although a_l is generally a complex number, we assume it to be real at $x = 0$ in order to avoid the biorthogonal functions needed for dealing with complex-valued HG functions [38]. Hermite polynomials $\mathcal{H}_p(\cdot)$ are given by

$$\mathcal{H}_p(\zeta) \;=\; (-1)^q e^{\zeta^2/2}\frac{d^q}{d\zeta^q}\left(e^{-\zeta^2/2}\right) \qquad \text{for} \quad q \,\in\, \mathbb{N}_0\,. \tag{38}$$

When $z = 0$, the magnetic field components H_x and H_y vanish and, therefore, we have a TE laser polarization compatible with the picture used in defining our 2-D model. The longitudinal modes β_p depend on p as follows

$$\beta_p^2 \;=\; k_0^2 n_e^2 \;-\; \alpha\left(p \,+\, \frac{1}{2}\right) \qquad \text{for} \quad p \,\in\, \mathbb{N}_0\,, \tag{39}$$

where n_e is the effective refractive index obtained as described in [39] for the case of InGaAsP. By using Equation (35c), the normalized magnetic lateral modes for H_z are

$$h_p(y) \;:=\; \frac{2}{\sqrt{3}(2p^2+2p+1)^{1/2}}\left(2p+1-\frac{\alpha}{2}y^2\right)\psi_p(y)\,, \tag{40}$$

derived from the generating function and orthogonality relations for HG polynomials (see Appendix .1).

3.2 Eigenfunction expansion at the laser output Γ_l

Laser radiation in Ω_{laser} is a linear combination of the aforementioned modes. When the beam is scattered by the PC, some of the radiation will re-enter into Ω_{laser} as

$$U_{\text{laser}}^{\text{sc}}(x,y) \;=\; \sum_{q\,=\,0}^{\infty} d_q\, h_q(y)\, e^{-\imath\beta_q x} \qquad x \,\leq\, 0\,, \quad y \in \mathbb{R}\,, \tag{41}$$

where $(h_q(y), \beta_q)_{q\in\mathbb{N}_0}$ represent the eigenpairs. The negative sign in the phase factor is due to the radiation reflected at the interface and transmitted from the exterior. As described in Section 2.5, the total laser field U_{laser} is divided in incoming and scattered parts, $U^{\text{inc}}_{\text{laser}}$ and $U^{\text{sc}}_{\text{laser}}$, respectively, with $U^{\text{inc}}_{\text{laser}}$ being the radiation in Ω_{laser} travelling from minus infinity to Γ_l along $\mathbf{e}_x$. We now require a description for the trace of $U^{\text{sc}}_{\text{laser}}(x,y)$ on Γ_l, $u^{\text{sc}}_l(y)$ as defined in Equation (29).

Coefficients $\{d_q\}_{q\in\mathbb{N}_0}$ can be obtained by taking the inner product between $U^{\text{sc}}_{\text{laser}}$ with a mode h_p, $p\in\mathbb{N}_0$ along any line with constant x. In particular, let us choose $x=0$ or Γ_l, and denote the inner product here by $\langle\cdot,\cdot\rangle$. Then,

$$\langle u^{\text{sc}}_l, h_p\rangle \;=\; \left\langle U_{\text{laser}}(0,\cdot) - U^{\text{inc}}_{\text{laser}}(0,\cdot), h_p\right\rangle \;=\; \sum_{q\,=\,0}^{\infty} d_q\,\langle h_q, h_p\rangle \tag{42}$$

according to the definitions given in Equations (25) and (29). The set of modes $\{h_p\}_{p\in\mathbb{N}_0}$ are not entirely orthogonal but their inner product yields a banded square matrix (see Appendix .1), denoted

$$\mathsf{H}_\infty \;=\; [\,\langle h_q, h_p\rangle\,]^{\infty,\infty}_{q,p=0}\;. \tag{43}$$

Hence, we can obtain the series coefficients via the unknown u^{sc}_l through the vector-matrix product

$$[\,d_q(u^{\text{sc}}_l)\,]^{\infty}_{q=0} \;=\; \mathsf{H}^{-1}_{\infty}\,[\langle u^{\text{sc}}_l, h_p\rangle]^{\infty}_{p=0}\;. \tag{44}$$

Using the above in Equation (41) yields the truncated series for the scattered field in the entire domain Ω_{laser}:

$$U^{\text{sc}}_{\text{laser}}(x,y) \;:=\; \sum_{q\,=\,0}^{\infty} d_q(u^{\text{sc}}_l)\,h_q(y)\,e^{-\imath\beta_q x} \tag{45}$$

where the dependence on u^{sc}_l is made explicit. Deriving Equation (45) along x yields

$$\frac{\partial U^{\text{sc}}_{\text{laser}}}{\partial x}(x,y) \;=\; -\sum_{q\,=\,0}^{\infty} \imath\beta_q d_q(u^{\text{sc}}_l)\,h_q(y)\,e^{-\imath\beta_q x} \qquad \text{for} \quad (x,y)\,\in\,\Omega_{\text{laser}}\,, \tag{46}$$

whose trace at Γ_l becomes

$$\frac{\partial U^{\text{sc}}_{\text{laser}}}{\partial x}(0,y) \;=\; -\sum_{q\,=\,0}^{\infty} \imath\beta_q d_q(u^{\text{sc}}_l)\,h_q(y) \qquad \text{for} \quad y\,\in\,\mathbb{R}\,. \tag{47}$$

This defines a DtN operator, denoted $\mathsf{T}^{\text{TE}}_l : H^{1/2}(\Gamma_l) \to H^{-1/2}(\Gamma_l)$, acting on u^{sc}_l. By Equation (32b), restriction to Γ_{li} delivers an expression for ψ^{TE}_{li},

$$\psi^{\text{TE}}_{li}(y) \;=\; \frac{\epsilon}{\epsilon_{\text{laser}}}\mathsf{T}^{\text{TE}}_l\,(u^{\text{sc}}_l)\,(y) \;=\; -\frac{\epsilon}{\epsilon_{\text{laser}}}\sum_{q\,=\,0}^{\infty} \imath\beta_q d_q(u^{\text{sc}}_l)\,h_q(y) \qquad \text{for} \quad |y| \,<\, R\,. \tag{48}$$

Notice that the operator T^{TE}_l maps u^{sc}_l, which is defined over the entire Γ_l and not its restriction to Γ_{li}, φ_{li}.

3.3 Eigenfunction expansion for the field on Ω_∞

The solution for the outgoing scattered field over the infinite domain Ω_∞ or *exterior solution* can be also expressed as an eigenfunction expansion of the isotropic half-plane problem [40]:

$$U_\infty^{\rm sc}(r,\theta) \;=\; \sum_{m=-\infty}^{\infty} b_m\, H_m^{(1)}(k_0\sqrt{\epsilon_\infty}\, r) e^{\imath m\theta} \qquad \text{for} \qquad r \,\geq\, R\,,\; 0 \,\leq\, \theta \,\leq\, \pi\,, \tag{49}$$

where R is the radius of the encircling frontier Γ_R and $H_m^{(1)}$ is the first type Hankel function of order m. From the first boundary condition in (P_∞), it holds

$$U_\infty^{\rm sc}(r,0) \;=\; U_\infty^{\rm sc}(r,\pi) \;=\; 0 \qquad \forall\, r \,\geq\, R\,. \tag{50}$$

Replacing this into Equation (49) shows that both conditions are linearly dependent since the Hankel functions satisfy

$$H_{-m}^{(1)}(\xi) \;=\; (-1)^m\, H_m^{(1)}(\xi)\,. \tag{51}$$

After some algebra, it is possible to write the above expansion as

$$\sum_{m=-\infty}^{\infty} b_m H_m^{(1)}(k_0\sqrt{\epsilon_\infty} r) \;=\; b_0\, H_0^{(1)}(k_0\sqrt{\epsilon_\infty} r) + \sum_{m=1}^{\infty} [b_m + (-1)^m b_{-m}]\, H_m^{(1)}(k_0\sqrt{\epsilon_\infty} r) \tag{52}$$

which vanishes for $r \,\geq\, R$, so that $b_0 \,=\, 0$ and $b_{-m} \,=\, -\, b_m (-1)^m$. When replaced in Equation (49) they render

$$U_\infty^{\rm sc}(r,\theta) \;=\; \sum_{m=1}^{\infty} \imath\, 2 b_m H_m^{(1)}(k_0\sqrt{\epsilon_\infty} r)\, \sin(m\theta)\,. \tag{53}$$

Equation (28a) together with the orthogonality relation for sinusoidal functions yields

$$\int_0^{2\pi} U_\infty^{\rm sc}(r,\theta) \sin(m\theta) d\theta \;=\; \imath\, 2\pi\, b_m\, H_m^{(1)}(k_0\sqrt{\epsilon_\infty}\, r)\,. \tag{54}$$

By choosing $r = R$, the coefficient b_m can be obtained as a function of the trace unknown φ_R introduced in (28a). Thus, for all $r \,\geq\, R$ it holds

$$U_\infty^{\rm sc}(r,\theta) \;=\; \sum_{m=1}^{\infty} \frac{\gamma_m(r)}{k_0\sqrt{\epsilon_\infty}} \sin(m\theta) \int_0^{2\pi} \varphi_R(\theta)\, \sin(m\theta') d\theta' \tag{55}$$

with

$$\gamma_m(r) \;:=\; \frac{k_0\sqrt{\epsilon_\infty}}{\pi} \frac{H_m^{(1)}(k_0\sqrt{\epsilon_\infty}\, r)}{H_m^{(1)}(k_0\sqrt{\epsilon_\infty}\, R)} \tag{56}$$

and whose radial derivative, corresponding to the direction of $-\mathbf{n}_\infty$, is

$$\frac{\partial U_\infty^{\rm sc}}{\partial r}(r,\theta) \;=\; \sum_{m=1}^{\infty} \gamma_m'(r) \sin(m\theta) \int_0^{2\pi} \varphi_R(\theta)\, \sin(m\theta') d\theta'\,. \tag{57}$$

The trace of the normal derivative of Equation (57) gives the Dirichlet-to-Neumann operator at Γ_R:

$$\mathsf{T}_R : \; H^{1/2}(\Gamma_R) \;\longrightarrow\; H^{-1/2}(\Gamma_R) \tag{58}$$

or, in other words, it provides the link between φ_R and ψ_R:

$$\psi_R \;=\; \mathsf{T}_R(\varphi_R) \;=\; \left.\frac{\partial U_\infty^{\rm sc}}{\partial r}\right|_{r=R} \tag{59}$$

which is independent on the polarization since the boundary is artificial. This kind of non-local DtN or non-reflecting boundary condition has been extensively studied in [43, 44, 45]. Explicitly,

$$\psi_R(\theta) \;=\; \sum_{m\,=\,1}^{\infty} \gamma_m'(r)\sin(m\theta)\int_0^{2\pi} \varphi_R(\theta)\,\sin(m\theta')d\theta' \qquad \text{for} \quad 0 \,\leq\, \theta \,\leq\, \pi\,. \tag{60}$$

3.4 Variational formulation for the interior problem

We now focus on $\Omega_{\rm int}$ where both operators $\mathsf{T}_l^{\rm TE}(u_l^{\rm sc})$ and $\mathsf{T}_R(\varphi_R)$ show up via boundary integrals which follow from the analysis below. Let us introduce the following variational forms defined for $H^1(\Omega_{\rm int})$-fields:

$$\mathsf{K}(U,V) \;:=\; \int_{\Omega_{\rm int}} a(\mathbf{x})\nabla U(\mathbf{x})\cdot\nabla V(\mathbf{x})\,d\Omega\,, \tag{61a}$$

$$\mathsf{M}(U,V) \;:=\; \int_{\Omega_{\rm int}} b(\mathbf{x})U(\mathbf{x})V(\mathbf{x})\,d\Omega\,, \tag{61b}$$

$$\mathsf{B}(U,V) \;:=\; \int_{\partial\Omega_{\rm int}} a(s)\frac{\partial U}{\partial n}(s)V(s)ds\,. \tag{61c}$$

After applying Green's first theorem, the weak form of $(P_{\rm int})$ for both polarization reads: find $U \in H^1(\Omega_{\rm int})$ such that

$$-\mathsf{K}(U,W) \;+\; \mathsf{B}(U,W) \;+\; k_0^2\mathsf{M}(U,W) \;=\; 0 \tag{62}$$

for all test functions in $W \in H^1(\Omega_{\rm int})$. The boundary integral can be split in Γ_{li} and Γ_R, and after replacing boundary conditions, one obtains

$$\int_{\Gamma_{li}} a(s)\frac{\partial U_{\rm int}}{\partial n}(s)W(s)\,ds \;=\; \int_{\Gamma_{li}} a(s)\left\{\frac{\partial U_{\rm int}^{\rm inc}}{\partial n}(s) \;+\; \psi_{li}(s)\right\}W(s)ds\,, \tag{63a}$$

$$\int_{\Gamma_R} a(s)\frac{\partial U_{\rm int}}{\partial n}(s)W(s)ds \;=\; \int_{\Gamma_R} a(s)\left\{\frac{\partial U_{\rm int}^{\rm inc}}{\partial n}(s) \;+\; \psi_R(s)\right\}W(s)ds\,. \tag{63b}$$

In order to apply the FEM, the scattered fields are expressed in terms of U and $U^{\rm inc}$ as shown in the following section. Henceforth, we consider coefficients a, b for the TE polarization case as given in Equation (15). The form of $U^{\rm inc}$ is precised in Appendix .2.

3.5 Reconstruction of the total field in Ω_{int}

If one desires to obtain the entire field U_{int}, expressions for the scattered fields ψ_{li}^{TE} and ψ_R, (85) and (59), respectively, must be written in terms of differences between total and incident fields on each corresponding subdomain. This yields,

$$\psi_R \;=\; \mathsf{T}_R(\varphi_R) \;=\; \mathsf{T}_R\left(\left\{U_\infty - U_\infty^{\text{inc}}\right\}\big|_{\Gamma_R}\right)\,, \tag{64}$$

$$\psi_{li}^{\text{TE}} \;=\; \frac{\epsilon}{\epsilon_{\text{laser}}}\mathsf{T}_l^{\text{TE}}(u_l^{\text{sc}})\big|_{\Gamma_{li}} \;=\; \frac{\epsilon}{\epsilon_{\text{laser}}}\mathsf{T}_l^{\text{TE}}\left(\left\{U_{\text{laser}} - U_{\text{laser}}^{\text{inc}}\right\}\big|_{\Gamma_l}\right)\Big|_{\Gamma_{li}}\,, \tag{65}$$

which can be left in terms of traces of U_{int} and $U_{\text{int}}^{\text{inc}}$ by Dirichlet transmission conditions (20). Thus, the corresponding boundary terms in (63a), (63b) become

$$\begin{aligned}
\int_{\Gamma_{li}} \epsilon^{-1}\psi_{li}^{\text{TE}} W ds \;&=\; \int_{\Gamma_{li}} \epsilon_{\text{laser}}^{-1}\mathsf{T}_l^{\text{TE}}\left(U_{\text{int}}\big|_{\Gamma_l}\right) W ds \;-\; \int_{\Gamma_{li}} \epsilon_{\text{laser}}^{-1}\mathsf{T}_l^{\text{TE}}\left(U_{\text{int}}^{\text{inc}}\big|_{\Gamma_l}\right) W ds\,,\\
\int_{\Gamma_R} \epsilon^{-1}\psi_R W\, ds \;&=\; \int_{\Gamma_R} \epsilon^{-1}\mathsf{T}_R\left(U_{\text{int}}\big|_{\Gamma_R}\right) W\, ds \;-\; \int_{\Gamma_R} \epsilon^{-1}\mathsf{T}_R\left(U_{\text{int}}^{\text{inc}}\big|_{\Gamma_R}\right) W ds\,.
\end{aligned} \tag{66}$$

Along with integrals of $\dfrac{\partial U_{\text{int}}^{\text{inc}}}{\partial n}$ in (63a) and (63b), the second terms in the right-hand side of (66) also represent sources. With this, we are ready to discretize and numerically solve our model.

4 Hybrid Finite Element / Boundary Element Model

4.1 Finite element formulation on Ω_{int}

Let $\left\{\Omega_{\text{int}}^h\right\}_h$ denote the family of triangular meshes of Ω_{int}, with exterior boundary $\partial\Omega_{\text{int}}^h$. Moreover, $\left\{\Omega_\alpha^h\right\}_h$ describes the families of subsets of Ω_{int}^h corresponding to discretizations of $\Omega_\alpha \subset \Omega_{\text{int}}$, such that they are mutually disjoint and their union yields

$$\bar{\Omega}_{\text{int}}^h \;=\; \bigcup_\alpha \bar{\Omega}_\alpha^h\,, \qquad \Omega_\alpha^h \cap \Omega_\beta^h \;=\; \emptyset \qquad \text{for} \quad \alpha \neq \beta\,. \tag{67}$$

If Ω_α^h and Ω_β^h are adjacent, their common boundaries are given by $\overline{\Omega}_\alpha^h \cap \overline{\Omega}_\beta^h$ (see Figure 4). This allows the immediate transfer of physical properties from Ω_α over each element of Ω_α^h.

We now construct a finite-element Galerkin formulation [40] over the interior domain Ω_{int}. Let W_j belong to the space of classic first-order polynomials, $\mathbb{P}_1(\bar{\Omega}_{\text{int}}^h)$, representing the test function for the j-th node with compact support in $\bar{\Omega}_{\text{int}}^h$. The continuous solution U_{int} is approximated by

$$U_{\text{int}}^h(\mathbf{x}) \;:=\; \sum_{i=1}^{N} \phi_i W_i(\mathbf{x}) \qquad \text{for} \quad \mathbf{x} \in \bar{\Omega}_{\text{int}}^h\,, \quad W_i \in \mathbb{P}_1\left(\bar{\Omega}_{\text{int}}^h\right). \tag{68}$$

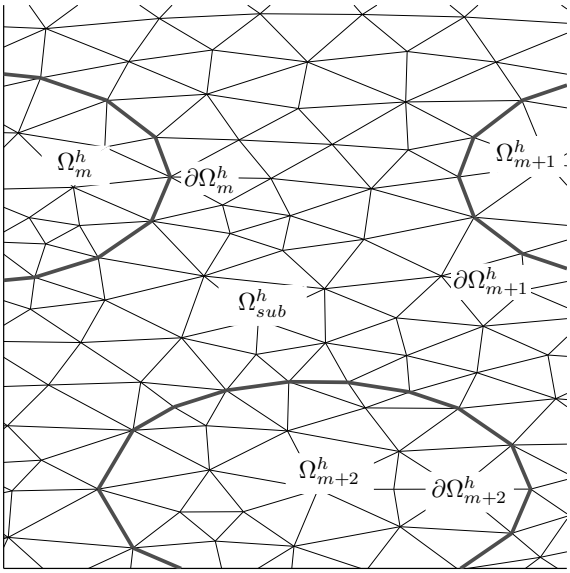

Figure 4: Triangular meshes Ω_m^h and Ω_{sub}^h corresponding to subdomains Ω_m and Ω_{sub}, respectively. Discrete interfaces are given by boundaries $\partial\Omega_m^h$.

where N denotes the number of nodes in Ω_{int}^h, proportional to h^{-1}, and ϕ_i are unknown field values at the nodes. We construct the following matrix entries coming from the variational form (62) and Equations (61a), (61b), (66):

Domain integrals:
$$(\mathsf{K})_{ij} := \int_{\Omega_{\text{int}}^h}\int_{\Omega_{\text{int}}^h} \epsilon^{-1}\nabla W_i \cdot \nabla W_j \, d\Omega \,, \tag{69a}$$
$$(\mathsf{M})_{ij} := \int_{\Omega_{\text{int}}^h}\int_{\Omega_{\text{int}}^h} W_i W_j \, d\Omega \,, \tag{69b}$$

Boundary integrals:
$$\left(\mathsf{B}_l^{\text{TE}}\right)_{ij} := \int_{\Gamma_{li}^h} \epsilon_{\text{laser}}^{-1} W_i \, \mathsf{T}_l^{\text{TE}}(W_j) \, ds \,, \tag{69c}$$
$$(\mathsf{B}_R)_{ij} := \int_{\Gamma_R^h} \epsilon^{-1} W_i \, \mathsf{T}_R(W_j) \, ds \,. \tag{69d}$$

Source terms are written as:

$$(\mathsf{S}_l)_i := \int_{\Gamma_{li}^h} W_i \left\{ \epsilon^{-1} \frac{\partial U_{\text{int}}^{\text{inc}}}{\partial n}\bigg|_{\Gamma_{li}^h} - \epsilon_{\text{laser}}^{-1} \mathsf{T}_l^{\text{TE}} \left(U_{\text{int}}^{\text{inc}}\big|_{\Gamma_{li}^h} \right) \right\} ds \,, \tag{70a}$$
$$(\mathsf{S}_R)_i := \int_{\Gamma_R^h} \epsilon^{-1} W_i \left\{ \frac{\partial U_{\text{int}}^{\text{inc}}}{\partial n}\bigg|_{\Gamma_R^h} - \mathsf{T}_R \left(U_{\text{int}}^{\text{inc}}\big|_{\Gamma_R^h} \right) \right\} ds \,. \tag{70b}$$

We then solve the linear system for coefficients ϕ_i:

$$\left(-\mathsf{K} + k_0^2\mathsf{M} + \mathsf{B}_l^{\text{TE}} + \mathsf{B}_R\right)\boldsymbol{\phi} = -\mathsf{S}_l - \mathsf{S}_R \tag{71}$$

where K and M are built by adding contributions for each node in accordance to a global node-numbering system. This yields a very sparse system but requires the identification of nodes along the boundaries. Moreover, the boundary integrals on Γ_{li}^h and Γ_R^h demand the derivation of *ad hoc* boundary elements defined as the traces of W_i, subject tackled next.

4.2 Boundary elements on Γ_R

The discrete version of (P_{int}) is coupled with the exterior problem (P_∞) through the line integrals in (70b) and (69d). Let the nodes describing Γ_R^h be identified by increasing angles $\{\theta_i\}_{i=0}^{N_R}$ counter-clockwise measured from the origin and where $N_R(h)+1$ denotes the total number of nodes dependent on h. Furthermore, assume the spacing between adjacent boundary nodes to be much smaller than the boundary radius R. Then, the test functions at the edges of Γ_R^h can be approximated as

$$W_i(r,\theta)\big|_{r=R} \;\approx\; \Theta_i(\theta) \;:=\; \begin{cases} \dfrac{\theta_{i+1} \,-\, \theta}{\Delta_{i+1}(\theta)} & \text{for} \quad \theta_i \,<\, \theta \,\leq\, \theta_{i+1}\ , \\ \dfrac{\theta \,-\, \theta_{i-1}}{\Delta_i(\theta)} & \text{for} \quad \theta_{i-1} \,<\, \theta \,\leq\, \theta_i\ , \\ 0 & \text{in any other case}\ , \end{cases} \tag{72}$$

and where we have defined the interval function $\Delta_i(\eta) := \eta_i - \eta_{i-1}$. Hence, the trace unknown φ_R can be approached by

$$\varphi_R^h \;:=\; \sum_{j\,=\,0}^{N_R} \phi_j\, \Theta_j(\theta) \qquad \text{for} \quad \theta \,\in\, (0,\pi)\ . \tag{73}$$

Recalling the form of $\mathsf{T}_R(\varphi_R)$ given by (60), we truncate the infinite series up to a certain bounded $N_\infty \in \mathbb{N}$ and define

$$\widetilde{\mathsf{T}}_R(\varphi_R^h) \;:=\; \sum_{m\,=\,1}^{N_\infty} \gamma_m\, \sin(m\theta) \left[\int_0^{2\pi} \sum_{j\,=\,0}^{N_R} \phi_j\, \Theta_j(\theta') \sin(m\theta') d\theta' \right] \tag{74}$$

wherein from (56), we have set $\gamma_m := \gamma_m'(R)$. Define the short-hand:

$$\sigma_j^m \;:=\; \int_{\theta_{j-1}}^{\theta_{j+1}} \Theta_j(\theta') \sin(m\theta') d\theta'\ , \qquad j \,=\, 1, \ldots, N_R - 1\ , \tag{75a}$$

$$\sigma_0^m \;:=\; \int_{\theta_0}^{\theta_1} \Theta_0(\theta') \sin(m\theta') d\theta'\ , \tag{75b}$$

$$\sigma_{N_R}^m \;:=\; \int_{\theta_{N_R-1}}^{\theta_{N_R}} \Theta_{N_R}(\theta') \sin(m\theta') d\theta'\ , \tag{75c}$$

whose computation is given in Appendix .3. Since the problem at hand considers only a half-circumference, (74) is turned into

$$\widetilde{\mathsf{T}}_R(\varphi_R^h) \;=\; \sum_{j\,=\,0}^{N_R} \phi_j \sum_{m\,=\,1}^{N_\infty} \gamma_m\, \sin(m\theta) \sigma_j^m \;=\; \sum_{j\,=\,0}^{N_R} \phi_j \widetilde{\mathsf{T}}_R(\Theta_j)(\theta) \tag{76}$$

for $\theta \in (0,\pi)$. Consequently, replacing test functions Θ_i in (69d) renders the contributions:

$$(\mathsf{B}_R)_{ij} \;=\; \int_{\theta_{i-1}}^{\theta_{i+1}} \epsilon^{-1}\Theta_i(\theta)\,\widetilde{\mathsf{T}}_R(\Theta_j)(\theta)Rd\theta\;, \qquad i\,=\,1,\ldots,\,N_R-1\;, \tag{77a}$$

$$(\mathsf{B}_R)_{0j} \;=\; \int_{\theta_0}^{\theta_1} \epsilon^{-1}\Theta_0(\theta)\,\widetilde{\mathsf{T}}_R(\Theta_j)(\theta)Rd\theta\;, \tag{77b}$$

$$(\mathsf{B}_R)_{N_Rj} \;=\; \int_{\theta_{N_R-1}}^{\theta_{N_R}} \epsilon^{-1}\Theta_{N_R}(\theta)\,\widetilde{\mathsf{T}}_R(\Theta_j)(\theta)Rd\theta\;, \tag{77c}$$

for $0 \le j \le N_R$. Notice that the infinitesimal line segment ds is given by $Rd\theta$. Thus, since $\epsilon \equiv \epsilon_{\rm con}$, the matrix elements $(\mathsf{B}_R)_{ij}$ are

$$(\mathsf{B}_R)_{ij} \;=\; \frac{R}{\epsilon_{\rm con}}\sum_{m\,=\,1}^{N_\infty}\gamma_m\sigma_i^m\sigma_j^m\;, \qquad 0\,\le\,i,j\,\le\,N_R\;, \tag{78}$$

or in matrix product form

$$(\mathsf{B}_R)_{ij} \;=\; \frac{R}{\epsilon_{\rm con}}\boldsymbol{\sigma}_i^T\,{\rm diag}\,\{\gamma_m\}\,\boldsymbol{\sigma}_j\;, \qquad 0\,\le\,i,j\,\le\,N_R\;, \tag{79}$$

wherein, for fixed i, $\boldsymbol{\sigma}_i$ is the vector with entries σ_i^m, m running from one to N_∞, the superindex T denotes transposition, and ${\rm diag}\,\{\gamma_m\}$ is the diagonal matrix of size N_∞ with terms γ_m. This is directly implemented in the solving code. On the other hand, the non-homogeneous terms $(\mathsf{S}_R)_{i=1}^{N_R}$, defined in Equation (70b) are given by

$$(\mathsf{S}_R)_i \;=\; \int_{\Gamma_R^h}\epsilon^{-1}W_i\,\frac{\partial U_{\rm int}^{\rm inc}}{\partial n}ds\;-\;\int_{\Gamma_R^h}\epsilon^{-1}W_i\,\widetilde{\mathsf{T}}_R(U_{\rm int}^{\rm inc}\big|_{\Gamma_R^h})ds\;. \tag{80}$$

Replacing the truncated form of $\widetilde{\mathsf{T}}_R$ into the above yields

$$(\mathsf{S}_R)_i \;=\; \int_{\Gamma_R}\frac{W_i}{\epsilon}\frac{\partial U_{\rm int}^{\rm inc}}{\partial n}ds\;-\;\sum_{m\,=\,1}^{N_\infty}\gamma_m\int_{\Gamma_R}\frac{W_i}{\epsilon}\sin(m\theta)ds\int_0^{2\pi}U_{\rm int}^{\rm inc}(R,\theta')\,\sin(m\theta')d\theta' \tag{81}$$

which is turned into

$$(\mathsf{S}_R)_i \;=\; \frac{R}{\epsilon_{\rm con}}\int_{\theta_{i-1}}^{\theta_{i+1}}\Theta_i(\theta)\frac{\partial U_{\rm int}^{\rm inc}}{\partial n}(R,\theta)d\theta\;-\;\frac{R}{\epsilon_{\rm con}}\sum_{m\,=\,1}^{N_\infty}\gamma_m\sigma_i^m\int_0^{2\pi}U_{\rm int}^{\rm inc}(R,\theta')\sin(m\theta')d\theta' \tag{82}$$

valid for $i=1,\ldots,N_R-1$ and with corresponding modifications for $i=\{0,N_R\}$. An explicit expression for $\dfrac{\partial U_{\rm int}^{\rm inc}}{\partial n}$ is provided in (110).

4.3 Boundary elements on Γ_{li}

Interaction with the laser system over $\Omega_{\rm laser}$ is given by the boundary integrals (69c) and (70a). Following the same reasoning as before, the edge test functions

used in this case are the following linear polynomials

$$W_i(x,y)\big|_{x=0} \;=\; Y_i(y) \;=\; \begin{cases} \dfrac{y_{i+1}\,-\,y}{\Delta_{i+1}(y)} & y_i \,<\, y \,\leq\, y_{i+1}\,, \\ \dfrac{y\,-\,y_{i-1}}{\Delta_i(y)} & y_{i-1} \,<\, y \,\leq\, y_i\,, \\ 0 & \text{in any other case}\,, \end{cases} \tag{83}$$

y_i being the y-coordinate of the i-th node, $i = 0, \ldots, N_{li}(h)$, over the discretized boundary Γ^h_{li}, $N_{li}(h)$ depending on mesh refinement. With this, φ_{li} is approximated by

$$\varphi^h_{li} \;:=\; \sum_{j\,=\,0}^{N_{li}} \phi_j Y_j(y)\,. \tag{84}$$

On the other hand, numerical implementation of the DtN operator $\mathsf{T}^{\mathrm{TE}}_l$ given in (48) requires truncating the series at a certain number $Q \in \mathbb{N}$ such that, for small $\varepsilon \,>\, 0$, $|d_q| \,<\, \varepsilon$ for all $q \,\geq\, Q$. This reduces the infinite dimensional matrix H_∞ from Equation (43) to a finite version denoted H_Q. Specific values of Q are discussed in Section 5.1. This yields the approximation

$$\widetilde{\mathsf{T}}^{\mathrm{TE}}_l(\varphi^h_{li})(y) \;=\; -\sum_{q\,=\,0}^{Q} \imath\beta_q d_q(\varphi^h_{li})\, h_q(y) \qquad \text{for} \quad |y| \,<\, R\,, \tag{85}$$

with $\{d_q\}_{q=0}^{Q}$ given by

$$\big[d_q(\varphi^h_{li})\big]_{q=0}^{Q} \;=\; \mathsf{H}_Q^{-1}\left[\langle \varphi^h_{li}, h_p\rangle\right]_{p=0}^{Q}\,. \tag{86}$$

Each entry of the vector on the right-hand side is given by the dot product:

$$\langle \varphi^h_{li}, h_p\rangle \;=\; \boldsymbol{\rho}^p \cdot \boldsymbol{\phi}\,, \qquad p = 0, \ldots, Q, \tag{87}$$

wherein we have defined the integrals

$$\rho^p_j \;=\; \langle Y_j(y), h_p\rangle \tag{88}$$

computed numerically via trapezoidal approximation. Hence, coming back to Equation (69c), and assuming $\epsilon_{\mathrm{laser}}$ constant, we obtain

$$\left(\mathsf{B}^{\mathrm{TE}}_l\right)_{ij} \;=\; \epsilon^{-1}_{\mathrm{laser}} \int_{\Gamma^h_{li}} Y_i \widetilde{\mathsf{T}}^{\mathrm{TE}}_l(Y_j)\, ds \;=\; -\epsilon^{-1}_{\mathrm{laser}} \int_{\Gamma^h_{li}} Y_i(y) \sum_{q\,=\,0}^{Q} \imath\beta_q d_q(Y_j)\, h_q(y)\, dy \tag{89}$$

which in matrix form becomes

$$\left(\mathsf{B}^{\mathrm{TE}}_l\right)_{ij} \;=\; \frac{-\imath}{\epsilon_{\mathrm{laser}}}\, \boldsymbol{\rho}^T_i \,\mathrm{diag}\,\{\beta_q\}\, \mathsf{H}_Q^{-1} \boldsymbol{\rho_j} \tag{90}$$

where $\mathrm{diag}\,\{\beta_q\}$ denotes the diagonal $(Q+1)$-matrix with terms equal to β_q, and the vector $\boldsymbol{\rho}_i$ has entries ρ^p_i, $p = 0, \ldots, Q$, for fixed i. Analogously, (70a) is approximated by

$$(\mathsf{S}_l)_i \;=\; \int_{\Gamma^h_{li}} Y_i \left\{ \epsilon^{-1} \frac{\partial U^{\mathrm{inc}}_{\mathrm{int}}}{\partial n}\bigg|_{\Gamma^h_{li}} \;-\; \epsilon^{-1}_{\mathrm{laser}}\, \widetilde{\mathsf{T}}^{\mathrm{TE}}_l \left(U^{\mathrm{inc}}_{\mathrm{int}}\big|_{\Gamma^h_l} \right) \right\} ds \tag{91}$$

for which the last term can be expressed as

$$\frac{-\imath}{\epsilon_{\text{laser}}}\,\boldsymbol{\rho}_i^T \operatorname{diag}\{\beta_q\}\,\mathsf{H}_Q^{-1}\left[\left\langle U_{\text{int}}^{\text{inc}}(0,\cdot),h_p\right\rangle\right]_{p=0}^{Q}\ . \tag{92}$$

In our numerical experiments, we will consider U^{inc} as the zeroth-order lasing mode, and consequently, the above expression simplifies to

$$(\mathsf{S}_l)_i \;=\; \frac{-2\imath}{\epsilon_{\text{laser}}}\beta_0\rho_i^0\ . \tag{93}$$

5 Simulation Parameters and Results

5.1 Laser and photonic crystal parameters

The choice of hexagonal symmetry for the photonic crystal corresponds to the overlap of PBGs for TM and TE polarizations in the infinitely periodic case. Particular PC parameters are designed to portray this bandgap at a central frequency $\lambda_o = 1.55\,\mu$m. For this, the ratio between the inclusions radii r and interhole spacing must be $r/a = 0.3$, and the substrate dielectric constant $\sqrt{\epsilon_{\text{con}}} = 2.65$, corresponding to the effective refraction index described in [13]. Under these conditions, the PBG for a infinite periodic crystal lies in the interval $\Delta\omega_{gap} = (a/\lambda_o) \approx 0.28 - 0.37$. However, these values are obtained assuming plane-wave propagation, and therefore, it is not the wavenumber k but the fast-propagating factor β_0 in the incoming wave that must correspond to the desired bandgap. Consequently, for the observation of frequency response, we sweep k so as to let β_0 lie on the desired interval and choose $a = 0.32\,\lambda_o$. Since only a finite number of unit cells are modeled, a complete PBG does not exist, i.e., evanescent modes are allowed to propagate. Examples of PCs and their dimensions are discussed in Section 5.5.

Laser parameters are based primarily on the work by [39] for the InGaAsP stripe geometry laser and have been summarized in Table 5.1. In practice, this parameters are only used for computing ϵ_{laser} and the factor α in the HG basis over Ω_{laser}.

5.2 Mesh parameters

Typical FE modeling of wave propagation along one direction requires a number of nodes per effective wavelength N_λ lying in the range between six and ten [45]. In our case, the effective wavelength λ_{con} is given over the connected domain Ω_{con} by $\lambda_{\text{con}} := \lambda_o/\sqrt{\epsilon_{\text{con}}}$. Hence, for the artifical boundary Γ_R radius, R, an accurate description of Ω_{int}, is achieved by $N \sim \pi N_\lambda^2 (R/\lambda_{\text{con}})^2$ nodes. In particular, for $R = 7\lambda_{\text{con}}$, the total number of nodes required should be around $N \sim 1.5 \times 10^4$, as observed in the error analysis below.

Clearly, the choice of R is key in determining computational costs. Physically, R has to be large enough to allow near-field effects to vanish and retain only the outgoing radiation, as it is the behavior prescribed over Γ_R. This asks for a sufficient free-propagation distance from the scattererers towards the artificial boundary of the order of λ_{con}. It also defines the length of Γ_{li} and so the number of wavelengths required to vanish away from the beam output. Consequently, R depends in a non-trivial fashion on the lattice dimensions, $w_{\text{pc}} \times l_{\text{pc}}$,

Parameter	Symbol	Value	Units
Free space wavenumber	k_0	4.05×10^6	m^{-1}
Longitudinal mode spacing	Δk	3.12×10^3	m^{-1}
Active layer thickness	d	0.20	μm
Laser width	w_l	400.00	μm
Cavity length	L	300	μm
Radiation confinement factor	Υ	0.47	-
Effective refractive index	n_e	3.54	-
Refractive index at cladding layers	n_1	3.36	-
Refractive index at active layer	n_2	3.74	-
Parabolic parameter	a_l	1.78×10^4	m^{-1}

Table 1: Laser parameters as given in [39].

the wavelength λ_{con}, and directly affects number of terms N_∞ and Q used in the trucated DtN operators $\widetilde{\mathsf{T}}_R$ and $\widetilde{\mathsf{T}}_l^{\mathrm{TE}}$.

5.3 Dirichlet-to-Neumann maps parameters

Under this heading we consider values for the truncation parameters N_∞ and Q of the DtNs previously defined in Sections 4.2 and 4.3, respectively. In the case of $\widetilde{\mathsf{T}}_R$, the general rule for bounded obstacles is [45]:

$$N_\infty \ \geq \ \lceil kR \rceil \tag{94}$$

which in the case of $R = 7\lambda_{\mathrm{con}}$ translates to $N_\infty \geq 44$. For the operator $\widetilde{\mathsf{T}}_l^{\mathrm{TE}}$ over Γ_l, minimal resolution is achieved for Q satisfying [41]

$$Q \ \geq \ \left\lceil \pi^2 \left[\frac{\max\{w_{\mathrm{pc}}, \lambda_{\mathrm{con}}\}}{\lambda_{\mathrm{con}}} \right]^2 \right\rceil \tag{95}$$

where w_{pc} is the photonic crystal width defined. Thus, even in the absence of scatterers we require $Q \geq 9$. Now, the conditioning number of the matrix H_Q deteriorates as Q increases and consequently an upper bound exists for numerical applications. This trade-off will be analyzed in the following section.

5.4 Model validation and error analysis

We validate our model by comparing it with known solutions, in particular, with the one in absence of scatterers and with results given in recent works. In the first case, the model does portray the incoming wave over Ω_{int}, defined in Appendix .2, as shown in Figure 5 for a suitable choice of parameters. Notwithstanding, numerical solutions reveal tails as well as a broader beam when compared to the analytical solution provided by [17], which is based on the paraxial approximation. This can explained by several reasons: (i) the paraxial approximation itself, as it is an approximation of the Helmholtz equation; (ii) mesh and truncation errors for the DtN operators; (iii) the degree of the polynomials used

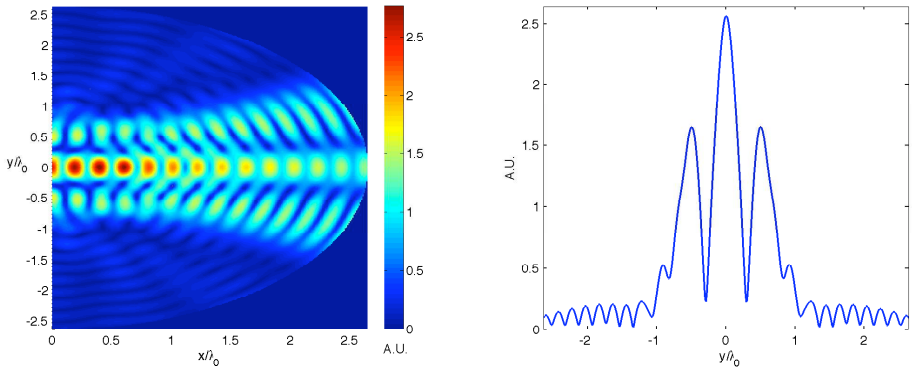

Figure 5: Absolute value and profile at Γ_{li} for the solution in absence of scatters with $N_\infty = 400$, $Q = 13$ and $N = 64433$. Remaining in oscillations towards the endpoints of Γ_{li} are due to the mismatch between T and $\mathsf{T}_l^{\mathrm{TE}}$ when approaching the y-axis.

for the FEM approximation; (iv) the different nature of the responses enforced at the boundaries Γ_{li} and Γ_R by the Dirichlet-to-Neumann operators. In what follows, we discuss the last three points.

Figure 6 shows the convergence rate for relative errors in L^2-norm for increasing number of nodes (decresing mesh parameter h) for different values of N_∞. As expected from standard FEM analysis, the convergence is algebraic in h due to the use of $\mathbb{P}_1$-bases. Consequently, better convergence rates can be expected if also p-refinements are employed. The lack of sensitivity in N_∞ is explained by the fact that measurements are taken in the L^2-norm and that the mesh has been refined above the threshold value given by the discrete inf-sup condition (see [45] for details).

In Figure 7, solutions are shown to converge as N_∞^{-1} for L^2-norms now taken on the boundary Γ_{li} regardless of Q. However, the offset does dependent greatly on the number of HG polynomials used. This reveals the interplay between both operators and becomes more relevant when dealing with highly oscillatory responses such as the ones produced by diffraction from the photonic crystal. One remedy is to increase the number of modes. Figure 8 reveals the necessity for Q larger than 40 to flatten out the profile as given by Equation (95) but for R larger than $7\lambda_{\mathrm{con}}$. In fact, the obtained results render the boundary condition $u_l = 0$ at $r > R$ inaccurate when R is not large enough. Thus, exchaging the Dirichlet condition over $\Gamma_{l\infty}$ by a mixed type or Robin type condition suggests a further improvement to the model. Nonetheless, results are still highly accurate in the range $20^{\mathrm{o}} \leq \theta \leq 160^{\mathrm{o}}$ [39].

5.5 Spatial response

As concrete examples, we consider the geometries depicted in Figure 9, denoted PC_3×11 and PC_4×13, wherein the connected areas are characterized by $\epsilon_{\mathrm{con}} = 2.65^2$, as mentioned before. In order to simplify the exposition, two cases will be treated for each configuration: identical inclusions or *full PC*, in which case $\epsilon_{\mathrm{base}} = \epsilon_{\mathrm{def}} = 1$; and, *PC with defect*, in which case inclusions lying along the

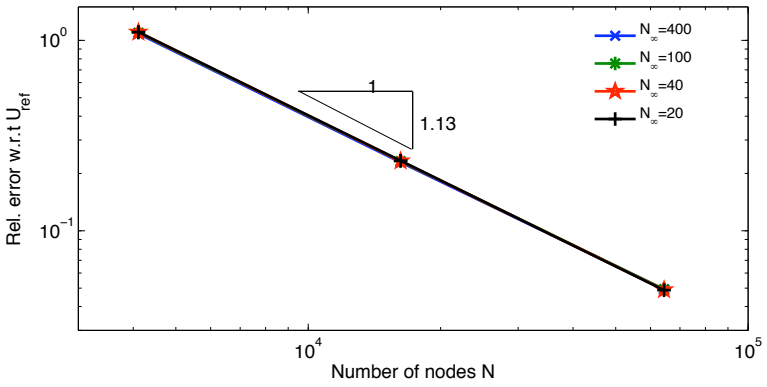

Figure 6: Number of nodes versus relative error in L^2-norm over Ω_{int} for different values of N_∞. The reference or overkill solution is taken at $N = 2.5 \times 10^5$ with $N_\infty = 400$ and $Q = 13$ in all cases.

line $y = 0$ take the permittivity value $\epsilon_{\text{def}} = \epsilon_{\text{con}}$. Program routines were written for MATLAB 7.4 by adaptating existing functions from the PDE toolbox, and tests were carried out in LINUX and MAC OSX operating systems running on laptop computers.

Let us first consider solutions for PC_3×11, as shown in Figures 10 and 11. Figure 10 shows absolute values for the computed total field U_{int} for full PC (left) and PC with defect (left) configurations. Clearly, a full lattice designed at the PBG will force the beam to remain contained near the output. Since the structure is not infinitely periodic, energy spreads symmetrically through the crystal along all possible column-free paths as observed both numerically and experimentally in [24], [22]. Figure 11 portrays traces u_{li} (left) and u_R (right) for solutions of the full PC (dashed line) and PC with defects (solid line). In the case of PC with defect, one observes a narrow beam at both Γ_{li} and Γ_R mostly due to the constructive superposition of scattered waves. On the right hand side of Figure 11, the difference between the intensity profiles when a defect is introduced is observed. Subwavelength focusing can be understood in this case by the collimation along the angle $\pi/2$. Given the direction of the crystal, the wave propagtes along the defect while at the same time narrowing the beam. Still, tails persist due to the mismatch between DtN operators at the endpoints of Γ_{li} and Γ_R.

In the case of PC_4×13, equivalent results are depicted in Figures 12 and 13. The main difference with respect to the previous configuration lies in the better definition of the laser beam when a defect is included. This somehow confirms the intuition that the more unit cells contained in the PC, the better the response. However, more energy is radiated towards Γ_{li} and consequently more polynomials are required to smooth out the response. Certainly, this imposes limits to the proposed model.

Though not presented at this time, changes in defect radii should be tried for smoothing the beam and a figure of merit for spatial-beam filter design should concern maximizing the ratio between the central part of the beam to the rest of it. Also, the present method allows for calculation of eigenvalues or resonances

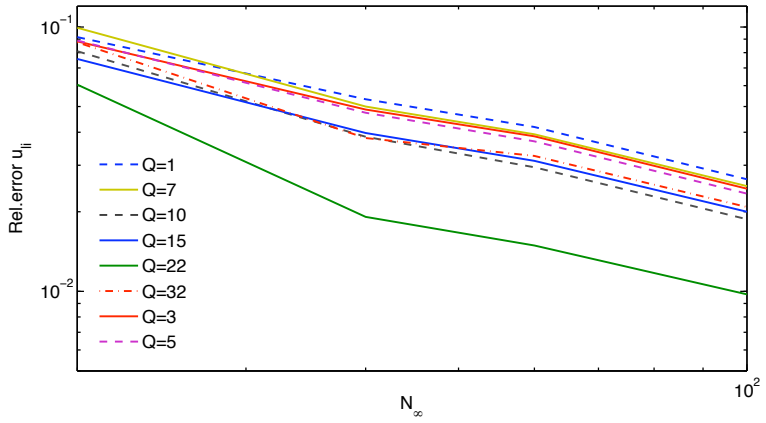

Figure 7: Number of truncature terms N_∞ with respect to relative error in L^2-norm over Γ_{li} for different values of Q. Reference solutions are taken for $N_\infty = 400$ and the total of mesh nodes is $N = 64433$.

inherent to the structure. These can be found by changing the condition at $\Gamma_{l\infty}$ so that the system becomes homogeneous, and hence an eigenvalue problem. Then, by sweeping the frequency and comparing the ratio between the maximum and minimum eigenvalues yielding an approximate location for resonances.

6 Concluding Remarks

We have presented a flexible model useful in the design of actual photonic structures by taking into account: (1) a finite periodic arrangement; (2) a simple implementation of radiation conditions at infinity for a half-space; and (3) the lasing modes allowed by a gain-guided DH laser. Boundary conditions were successfully implemented by use of Dirichlet-to-Neumann operators based on physical considerations (2) and (3) yielding expansion series of Hankel and Hermite-Gauss polynomials, respectively. In order to keep the problem complexity to a minimum, the HG polynomials were not allowed to take complex values though this could later on be developed by use of bi-orthogonal functions. Numerical results for simple cases were obtained by deriving a convenient variational formulation for the hybrid finite-element method using MATLAB. Error analyses on different truncation and meshing parameters was carried out.

Several ideas can be further developed. Among these, we will be interested in: (1) design figures for parameter optimization; (2) detailed analysis of spectral properties; (3) replacing h-based FEM by hp-refinements; (4) introduction of more accurate conditions on the laser interface as, for instance, impedance conditions that would give rise to so-called *surface or interfacial waves*; (4) use of local non-reflecting boundary conditions to increase efficiency over the artificial boundary; and (5) extension to $\mathbb{R}^3$ in order to account for the entire slab structure and vertical diffraction.

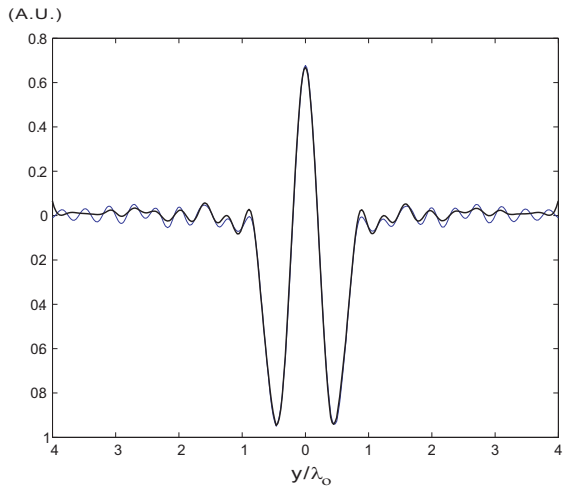

Figure 8: Smoothening out the tails: scatterer-free solution real-part profiles at Γ_{li} for $Q = 40$ (thin line) and $Q = 100$ (thick line) for k_0.

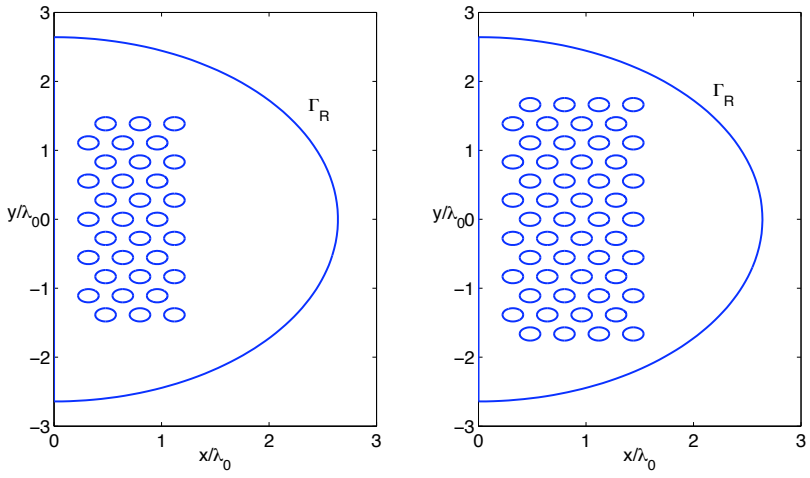

Figure 9: Test geometries for fixed parameters $R = 7\lambda_{\text{con}}$, and r, a, as defined in Section 5.1. On the left-hand side, configuration PC_3×11 contains with three layers of inclusions along x and eleven along y. On the right-hand side, the configuration PC_4×13 has corresponding numbers of layers. Defects are referred to inclusions lying along the $y = 0$ line.

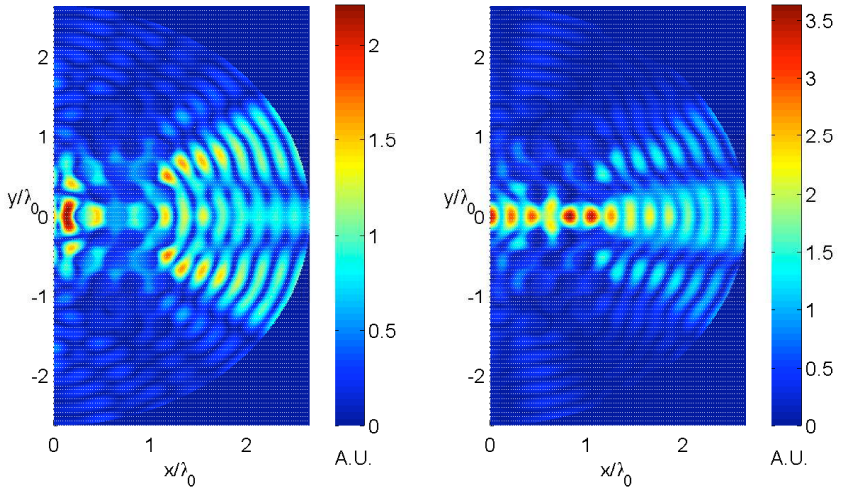

Figure 10: Absolute values for solutions of PC_3×11, $\epsilon_{\text{con}} = 2.65^2$ and $\epsilon_{\text{base}} = \epsilon_{\text{def}} = 1$ (left) , and with a defect on the central row $\epsilon_{\text{def}} = 2.65$ (right). Model parameters are $N = 51,245$, $N_\infty = 200$ and $Q = 23$.

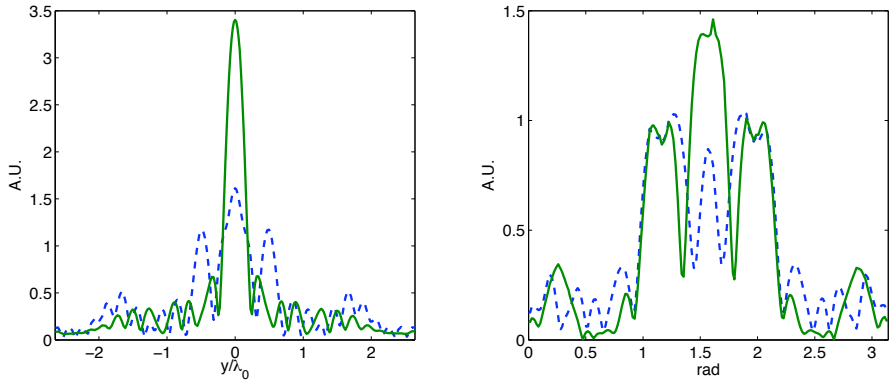

Figure 11: Solution profiles taken at Γ_{li} and Γ_R in absolute value for the full PC (dashed line) and PC with defect (solid line) configurations.

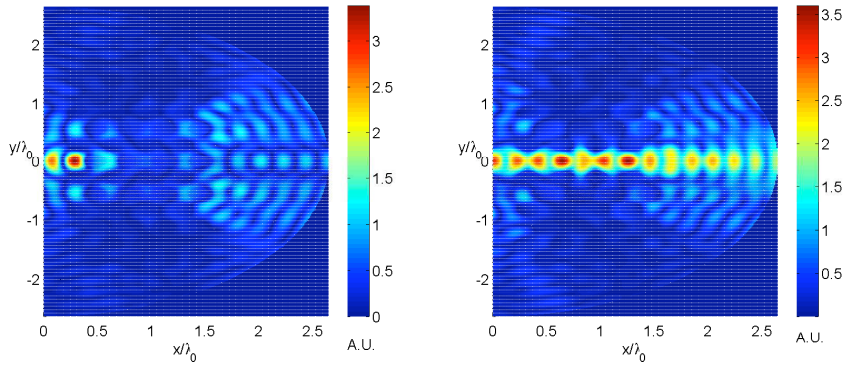

Figure 12: Absolute values for solutions of PC_4×13, $\epsilon_{\text{con}} = 2.65^2$ and $\epsilon_{\text{base}} = \epsilon_{\text{def}} = 1$ (left) , and with a defect on the central row $\epsilon_{\text{def}} = 2.65$ (right). Model parameters are $N = 63,363$, $N_\infty = 200$ and $Q = 27$.

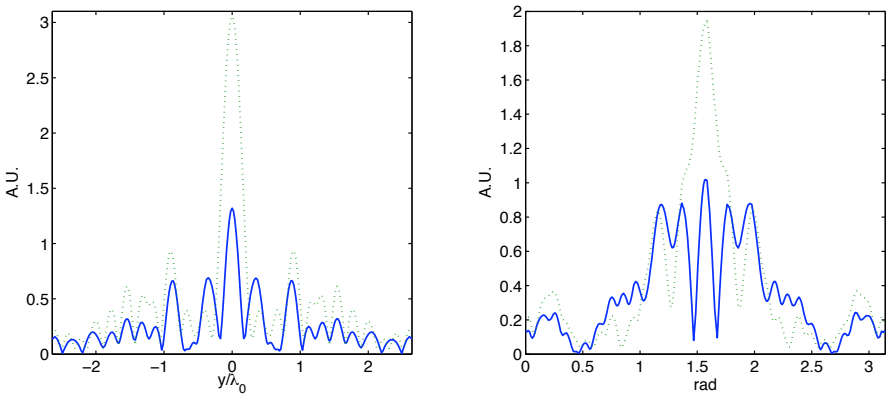

Figure 13: Solution profiles taken at Γ_{li} and Γ_R in absolute value for the full PC (solid line) and PC with defect (dashed line) configurations.

.1 Normalization of lateral modes $H_z^p(y)$

In Section 3.2, the normal component of the magnetic field is given by (35c), which after derivation yields

$$H_z^p(y,0) \;=\; \eta\left(2p \;+\; 1 \;-\; \frac{\alpha}{2}y^2\right)\frac{\psi_p(y)}{\beta_p} \tag{96}$$

where $\eta = \alpha/(\omega\mu_0)$ and $\alpha \;=\; 2k_0a_l\sqrt{\Upsilon}$ assumed to be real-valued. Thus,

$$\begin{aligned}\langle H_z^p, H_z^q\rangle \;&=\; \int_{-\infty}^{\infty} H_z^p(y,0)\,H_z^q(y,0)\,dy \\ &= \eta^2\Big[\,(2p\;+\;1)(2q\;+\;1)\left\langle\frac{\psi_p}{\beta_p},\frac{\psi_q}{\beta_q}\right\rangle -\;\alpha\,(p\;+\;q\;+\;1)\left\langle y^2\frac{\psi_p}{\beta_p},\frac{\psi_q}{\beta_q}\right\rangle \\ &\quad+\;\frac{1}{4}\alpha^2\left\langle y^2\frac{\psi_p}{\beta_p},y^2\frac{\psi_q}{\beta_q}\right\rangle\Big]\,.\end{aligned} \tag{97}$$

The first inner product gives

$$\left\langle\frac{\psi_p}{\beta_p},\frac{\psi_q}{\beta_q}\right\rangle \;=\; \begin{cases}\beta_p^{-2} & \text{if } q\;=\;p\,,\\ 0 & \text{any other case}\,.\end{cases} \tag{98}$$

The second one has an y^2 factor which can be separated so that

$$\left\langle y^2\frac{\psi_p}{\beta_p},\frac{\psi_q}{\beta_q}\right\rangle \;=\; \left\langle y\frac{\psi_p}{\beta_p},y\frac{\psi_q}{\beta_q}\right\rangle\,. \tag{99}$$

Replacing the actual expression for ψ, Equation (37), above and using the recurrence relation [42]:

$$\mathcal{H}_{p+1}(\xi)\;-\;\xi\mathcal{H}_p(\xi)\;+\;p\mathcal{H}_{p-1}(\xi)\;=\;0\,, \tag{100}$$

one obtains

$$\begin{aligned}y\psi_p(y) \;&=\; \frac{1}{\sqrt{\alpha}}\sqrt[4]{\frac{\alpha}{2\pi}}\sqrt{\frac{1}{p!}}\left(\mathcal{H}_{p+1}(y\sqrt{\alpha})\;+\;p\mathcal{H}_{p-1}(y\sqrt{\alpha})\right)e^{-\frac{1}{2}\alpha\,y^2} \\ &=\; \sqrt{\frac{p+1}{\alpha}}\,\psi_{p+1}(y)\;+\;\sqrt{\frac{p}{\alpha}}\,\psi_{p-1}(y)\,.\end{aligned} \tag{101}$$

Thus,

$$\left\langle y^2\frac{\psi_p}{\beta_p},\frac{\psi_q}{\beta_q}\right\rangle \;=\; \frac{1}{\alpha}\begin{cases}(2p+1)\beta_p^{-2} & \text{if } q\;=\;p\\ (p+1)^{1/2}(p+2)^{1/2}\beta_p^{-1}\beta_{p+2}^{-1} & \text{if } q\;=\;p+2\,,\\ p^{1/2}(p-1)^{1/2}\beta_p^{-1}\beta_{p-2}^{-1} & \text{if } q\;=\;p-2\,,\\ 0 & \text{any other case}\,.\end{cases} \tag{102}$$

For the third inner product in (97) a similar procedure is carried out as

$$y^2\psi_p \;=\; y\sqrt{\frac{p+1}{\alpha}}\,\psi_{p+1}\;+\;y\sqrt{\frac{p}{\alpha}}\,\psi_{p-1} \tag{103}$$

is turned into

$$y^2\psi_p \;=\; \frac{1}{\alpha}\left(\sqrt{p+1}\sqrt{p+2}\,\psi_{p+2} \;+\; (2p\;+\;1)\,\psi_p \;+\; \sqrt{p-1}\sqrt{p}\,\psi_{p-2}\right)\;. \quad (104)$$

Hence,

$$\left\langle y^2\frac{\psi_p}{\beta_p}, y^2\frac{\psi_q}{\beta_q}\right\rangle \;=\; \frac{1}{\alpha^2}\begin{cases}(6p^2+6p+3)\beta_p^{-2} & \text{if } q \;=\; p\;,\\ (4p+6)(p+1)^{1/2}(p+2)^{1/2}\beta_p^{-1}\beta_{p+2}^{-1} & \text{if } q \;=\; p+2\;,\\ (4p-2)p^{1/2}(p-1)^{1/2}\beta_p^{-1}\beta_{p-2}^{-1} & \text{if } q \;=\; p-2\;,\\ \sqrt{(p+4)!/p!}\beta_p^{-1}\beta_{p+4}^{-1} & \text{if } q \;=\; p+4\;,\\ \sqrt{p!/(p-4)!}/\beta_p^{-1}\beta_{p-4}^{-1} & \text{if } q \;=\; p-4\;,\\ \quad 0 & \text{any other case}\;.\end{cases} \quad (105)$$

Hence, taking the above along with expressions (98) and (102) into (97) gives

$$\langle H_z^p, H_z^p\rangle \;=\; \frac{3}{4}\frac{\eta^2}{\beta_p^2}(2p^2+2p+1)\;, \quad (106a)$$

$$\left\langle H_z^p, H_z^{p+2}\right\rangle \;=\; -\frac{\eta^2}{\beta_p\beta_{p+2}}\sqrt{p+1}\sqrt{p+2}\,(2p+3)\;, \quad (106b)$$

$$\left\langle H_z^p, H_z^{p-2}\right\rangle \;=\; \left\langle H_z^{p-2}, H_z^p\right\rangle \;=\; -\frac{\eta^2}{\beta_p\beta_{p-2}}\sqrt{p(p-1)}\,(2p-1)\;, \quad (106c)$$

$$\left\langle H_z^p, H_z^{p+4}\right\rangle \;=\; \frac{1}{4}\frac{\eta^2}{\beta_p\beta_{p+4}}\sqrt{\frac{(p+4)!}{p!}}\;, \quad (106d)$$

$$\left\langle H_z^p, H_z^{p-4}\right\rangle \;=\; \left\langle H_z^{p-4}, H_z^p\right\rangle \;=\; \frac{1}{4}\frac{\eta^2}{\beta_p\beta_{p-4}}\sqrt{\frac{p!}{(p-4)!}}\;. \quad (106e)$$

.2 Incident field. Paraxial approximation

Contrary to most models, we assume that the incident wave is an actual laser solution. In the isotropic case, analytic expressions can be obtained after carrying out the paraxial approximation, i.e., under the assumption that beams vary much faster along x than in y. Although this induces an error with respect to the actual Helmholtz solution, it has the advantage of being readily amenable for computational purposes. Thus, the incident wave is given by the first laser mode propagating in free space [17]:

$$U^{\text{inc}}(x,y) \;=\; \frac{2}{\sqrt{3}}\left(1\;-\;\frac{\alpha(x)}{2}y^2\right)\sqrt[4]{\frac{\alpha_0}{2\pi}}\left(\frac{q(0)}{q(x)}\right)^{1/2}\exp\left[\imath\beta_0 x - \imath\,\frac{\alpha(x)}{4}y^2\right] \quad (107)$$

where

$$\alpha(x) \;=\; \frac{2k_0\sqrt{\epsilon}}{q(x)}\;, \qquad q(x) \;=\; q(0)+x\;, \quad (108)$$

and $q(0)$ is the parameter value at Γ_{li}. In fact, the term $q(0)$ gives the beam waist at $x \;=\; 0$. In order to retrieve the incoming wave over Γ_R, we switch to

polar coordinates:

$$U^{\text{inc}}(r,\theta) \;=\; \frac{2}{\sqrt{3}}\left(1 \,-\, \frac{\alpha(r\sin\theta)}{2} r^2\cos^2\theta\right)\,\sqrt[4]{\frac{\alpha(r\sin\theta)}{2\pi}} \\ \times \exp\left[\imath\beta_0\, r\sin\theta - \imath\,\frac{\alpha(r\sin\theta)}{4} r^2\cos^2\theta\right] \tag{109}$$

Since $\mathbf{n} = \mathbf{r}/r$ over Γ_R, we obtain

$$\left.\frac{\partial U^{\text{inc}}}{\partial r}\right|_{\Gamma_R} = \frac{2}{\sqrt{3}}\sqrt[4]{\frac{\alpha}{2\pi}}\,\exp\left[\imath\beta_0\, R\sin\theta - \imath\,\frac{\alpha}{4}R^2\cos^2\theta\right] \times \Big[-\frac{\alpha'}{2}R^2\sin\theta\cos^2\theta \\ -\,\alpha R\cos^2\theta \,+\, \left(1 \,-\, \frac{\alpha}{2}R^2\cos^2\theta\right)\left(\frac{1}{4\alpha}\alpha'\sin\theta - \imath\beta_0\sin\theta\right) \\ -\,\imath\, R\cos^2\theta\left(1 \,-\, \frac{\alpha}{2}R^2\cos^2\theta\right)\left(\frac{\alpha'}{4}R\sin\theta \,+\, \frac{\alpha}{2}\right)\Big] \tag{110}$$

where $\alpha' \;=\; -2k_0\sqrt{\epsilon}/(q_0 + R\sin\theta)^2$

.3 Computation of terms σ_j^m

Coefficients σ_j^m are found by direct integration of the actual form of Θ_j, given in Equation (72),

$$\sigma_j^m \;=\; \int_{\theta_{j-1}}^{\theta_j} \frac{(\theta \,-\, \theta_{j-1})}{\Delta_j(\theta)}\sin(m\theta)d\theta \,+\, \int_{\theta_{j-1}}^{\theta_j} \frac{(\theta_{j+1} \,-\, \theta)}{\Delta_{j+1}(\theta)}\sin(m\theta)d\theta \tag{111}$$

Using formulae

$$\int_{\theta_a}^{\theta_b} \theta\sin(m\theta)d\theta \;=\; -\,\frac{\theta}{m}\cos(m\theta)\Big|_{\theta_a}^{\theta_b} \,+\, \frac{\sin(m\theta)}{m^2}\Big|_{\theta_a}^{\theta_b} \tag{112a}$$

$$\int_{\theta_a}^{\theta_b} \sin(m\theta)d\theta \;=\; -\,\frac{\cos(m\theta)}{m}\Big|_{\theta_a}^{\theta_b} \tag{112b}$$

the first term on the right-hand side of (111) is equal to

$$\int_{\theta_{j-1}}^{\theta_j} \frac{(\theta \,-\, \theta_{j-1})}{\Delta_j(\theta)}\sin(m\theta)d\theta \;=\; \frac{1}{\Delta_j(\theta)}\left[-\frac{\theta}{m}\cos(m\theta) \,+\, \frac{\sin(m\theta)}{m^2}\right]\Big|_{\theta_{j-1}}^{\theta_j} \\ +\;\frac{\theta_{j-1}}{\Delta_j(\theta)}\frac{\cos(m\theta)}{m}\Big|_{\theta_{j-1}}^{\theta_j} \tag{113}$$

which after rearranging terms becomes

$$\int_{\theta_{j-1}}^{\theta_j} \frac{(\theta \,-\, \theta_{j-1})}{\Delta_j(\theta)}\sin(m\theta)d\theta \;=\; -\frac{\cos(m\theta_j)}{m} \,+\, \frac{1}{\Delta_j(\theta)}\frac{\sin(m\theta)}{m^2}\Big|_{\theta_{j-1}}^{\theta_j} \tag{114}$$

Repeating the process for the second integral yields

$$\int_{\theta_j}^{\theta_{j+1}} \frac{(\theta_{j+1} \,-\, \theta)}{\Delta_{j+1}(\theta)}\sin(m\theta) \;=\; \frac{\cos(m\theta_j)}{m} \,-\, \frac{1}{\Delta_{j+1}(\theta)}\frac{\sin(m\theta)}{m^2}\Big|_{\theta_j}^{\theta_{j+1}} \tag{115}$$

Hence,

$$\sigma_j^m \;=\; \frac{1}{m^2}\left[\frac{\sin(m\theta)}{\Delta_j(\theta)}\Big|_{\theta_j-1}^{\theta_j} \;-\; \frac{\sin(m\theta)}{\Delta_{j+1}(\theta)}\Big|_{\theta_j}^{\theta_{j+1}}\right] \qquad 1 \le j \le N_R - 1 \qquad (116)$$

Expressions for σ_0^m and $\sigma_{N_R}^m$ are similarly obtained

$$\sigma_0^m \;=\; \frac{\cos(m\theta_0)}{m} \;-\; \frac{1}{\Delta_1(\theta)}\frac{\sin(m\theta)}{m^2}\Big|_{\theta_0}^{\theta_1} \qquad (117a)$$

$$\sigma_{N_R}^m \;=\; -\,\frac{\cos(m\theta_{N_R})}{m} \;+\; \frac{1}{\Delta_{N_R}(\theta)}\frac{\sin(m\theta)}{m^2}\Big|_{\theta_{N_R-1}}^{\theta_{N_R}} \qquad (117b)$$

References

[1] Yablonovitch E. Inhibited spontaneous emission in solid-state physics and electronics. *Physics Review Letters* 1987; **58**:2059–2062.

[2] Joannopoulos JD, Meade R, Winn J. *Photonic Crystals: Molding the Flow of Light*. Princeton University Press: New Jersey, 1995.

[3] Sakoda K. *Optical properties of Photonic Crystals*, Springer Series in Optical Sciences, vol. 80. Springer-Verlag: Berlin, 2001.

[4] John S. Strong localization of photons in certain disordered dielectric superlattices. *Physics Review Letters* 1987; **58**: 2486–2489.

[5] Fan S, Villeneuve P, Joannopoulos J, Haus H. Channel drop tunneling through localized states. *Physics Review Letters* 1998; **80**: 960–963.

[6] Noda S, Chutinan A, Imada M. Trapping and emission of photons by a single defect in a photonic bandgap structure. *Nature* 2000; **407**: 608–610.

[7] Busch K. Photonic band structure theory: assesment and perspectives. *Comptes Rendus Physique* 2002; **3**: 52–66.

[8] Kharkashadze D, Zaridze R, Bijamov A, Hafner C, Smajic J, Erni D. Reflection compensation scheme for the efficient and accurate computation of waveguide discontinuities in photonic crystals. *ACES Journal* 2004; **19**(1a): 10–21.

[9] Sanchis P, Bienstman P, Luyssaert B, Baets R, Marti J. Analysis of butt coupling in photonic crystals. *IEEE Journal of Quantum Electronics* 2004; **40**(5): 541–550.

[10] Kuchment P. The mathematics of photonic crystals. *Frontiers in Applied Mathematics, SIAM* 2001; **22**: 207–272.

[11] Johnson S, Joannopoulos JD. Block-iterative frequency-domain methods for Maxwell's equations in a planewave basis. *Optics Express* 2001; **8**(3): 173–190.

[12] Rodríguez-Esquerre V, Koshiba M, Hernández-Figueroa H. Finite-element time-domain analysis of 2-D photonic crystal resonant cavities. *IEEE Photonics Technology Letters* 2004; **16**: 816–818.

[13] Painter O, Vuckŏvić J, Scherer A. Defect modes of a two-dimensional photonic crystal in an optically thin dielectric slab. *Journal of Optical Society of America B* 1999; **16**: 275–285.

[14] Lu M, Shanker B, Michielssen E. Elimination of spurious solutions associated with exact transparent boundary conditions in FDTD solvers. *IEEE Antennas And Wireless Propagation Letters* 2004; **3**(4): 59–62.

[15] Wu JH, Liu AQ, Ang LK, Cheng TH, Xu K, Wu J, Lin JT. Complex photonic band diagrams for finite-size photonic crystals with arbitrary defects. *Journal of Applied Physics* 2007; **101**: 053101

[16] Verdeyen JT. *Laser Electronics* (3rd edn)., Prentice Hall series in solid state physical electronics. Prentice Hall: New Jersey, 1995.

[17] Siegman AE. *Lasers*. University Science Books: Mill Valley, 1986.

[18] Cook D, Nash F. Gain-induced guiding and astigmatic output beam of Ga-As lasers. *Journal of Applied Physics* 1975; **46**: 1660–1672.

[19] Yariv A. *Optical Electronics in Modern Communications* (5th edn), The Oxford Series in Electrical and Computer Engineering. Oxford University Press: New Yok, 1997.

[20] Meystre P, Sargent M. *Elements of Quantum Optics* (3rd edn) Springer-Verlag: Berlin,1999.

[21] Saleh B, Teich M. *Fundamentals of Photonics*, Wiley series in pure and applied optics. John Wiley & Sons, Inc.:New York, 1991.

[22] Cubukcu E, Aydin K, Ozbay E, Foteinopolou S, Soukoulis CM. Subwavelength resolution in a two-dimensional photonic-crystal-based superlens. *Physical Review Letters* 2003; **91**(20): 207401

[23] Kramper P, Agio M, Soukoulis CM, Birner A, Müller F, Wehrspohn RB, Gosele U, Sandoghdar. Highly directional emission from photonic crystal waveguides of subwavelength width. *Physical Review Letters* 2004; **92**(11): 113903.

[24] Ozbay E, Aydin K, Bulu I, Guven K. Negative refraction, subwavelength focusing and beam formation by photonic crystals *Journal of Physics D: Applied Physics* 2007; **40**: 2652–2658

[25] Zienkiewicz OC, Kelly DW, Beitess P. The coupling of the finite element method and boundary solution procedures. *International Journal for Numerical Methods in Engineering* 1977; **11**(4): 355–375.

[26] Brezzi F, Johnson C. On the coupling of boundary integral and finite element methods. *Calcolo* 1979; **16**(2): 189–201.

[27] Johnson C, Nédélec JC. On the coupling of boundary integral and finite element methods. *Mathematics of Computation* 1980; **35**(152): 1063–1079.

[28] Stephan E. Coupling of finite elements and boundary elements for some nonlinear interface problems. *Computational Methods in Applied Mechanics and Engineering* 1992; **101**(2–3): 61–72.

[29] Li ZC, Lu TT. Singularities and treatments of elliptic boundary value problems. *Mathematical and Computer Modelling* 2000; **31**(8): 97–145.

[30] Bossavit A. Mixed methods and the marriage between mixed finite elements and boundary elements. *Numerical Methods for Partial Differential Equations* 2005; **7**(4): 347–362.

[31] Jackson JD. *Classical Electrodynamics* (3rd edn). John Wiley & Sons, Inc.: New York, 1999.

[32] McLean, W. *Strongly Elliptic Systems and Boundary Integral Equations*. Cambridge University Press: New York, 2000.

[33] Butler JK, Delaney JB. A rigorous boundary value solution for the lateral modes of stripe geometry injection lasers. *IEEE Journal of Quantum Electronics* 1978; **14**: 507–513.

[34] Butler JK, Delaney JB. Field solutions for the lateral modes of stripe geometry injection lasers. *IEEE Journal of Quantum Electronics* 1980; **16**: 1326–1328.

[35] Mansuripur M, Wright EM. The optics of semiconductor diode lasers. *Optics & Photonics News* 2002; (july): 57–61.

[36] Agrawal GP, Dutta NK. *Semiconductor Lasers* (2nd edn). Van Nostrand Reinhold: New York, 1993.

[37] Paoli TL. Waveguiding in a stripe-geometry junction laser. *IEEE Journal of Quantum Electronics* 1977; **13**: 662–668.

[38] Kostenbauder A, Sun Y, Siegman AE. Eigenmode expansions using biorthogonal functions: complex-valued Hermite-Gaussians. *Journal of Optical Society of America* 1997; **14**: 1780–1790.

[39] Botez D. InGaAsP/InP double-heterostructure lasers: Simple expressions for wave confinement, beamwidth, and threshold current over wide ranges in wavelength (1.1-1.65 μm). *IEEE Journal of Quantum Electronics* 1981; **17**(2): 178–186.

[40] Jin J. *The Finite Element Method in Electromagnetics*. John Wiley & Sons, Inc.: New York, 2002.

[41] Someda C. *Electromagnetic Waves* (2nd edn). CRC Press: Boca Raton, 2006.

[42] Hochstadt H. *The Functions of Mathematical Physics*. Dover Publications, Inc.: New York, 1986.

[43] Givoli D. *Numerical Methods for Problems in Infinite Domains*. Elsevier: Amsterdam, 1992.

[44] Givoli D, Patlashenko I, Keller, JB. High-order boundary conditions and finite elements for infinite domains. *Computational Methods in Applied Mechanics and Engineering* 1997; **143**: 13–39.

[45] Ihlenburg F. *Finite Element Analysis of Acoustic Scattering*, Series on Applied Mathematical Sciences, vol. 132 Springer-Verlag: New York, 1998.

Research Reports

No.	Authors/Title
09-25	*M. Durán, M. Guarini, C.F. Jerez-Hanckes* Hybrid FEM/BEM modeling of finite-sized photonic crystals for semiconductor laser beams
09-24	*A. Bespalov, N. Heuer, R. Hiptmair* Convergence of the natural *hp*-BEM for the electric field integral equation on polyhedral surfaces
09-23	*R. Hiptmair, J. Li, J. Zou* Real interpolation of spaces of differential forms
09-22	*R. Hiptmair, J. Li, J. Zou* Universal extension for Sobolev spaces of differential forms and applications
09-21	*T. Betcke, D. Kressner* Perturbation, computation and refinement of invariant pairs for matrix polynomials
09-20	*R. Hiptmair, A. Moiola and I. Perugia* Plane wave discontinuous Galerkin methods for the 2D Helmholtz equation: analysis of the p–version
09-19	*C. Winter* Wavelet Galerkin schemes for multidimensional anisotropic integrodifferential operators
09-18	*C.J. Gittelson* Stochastic Galerkin discretization of the lognormal isotropic diffusion problem
09-17	*A. Bendali, A. Tizaoui, S. Tordeux, J. P. Vila* Matching of Asymptotic Expansions for a 2-D eigenvalue problem with two cavities linked by a narrow hole
09-16	*D. Kressner, C. Tobler* Krylov subspace methods for linear systems with tensor product structure
09-15	*R. Granat, B. Kågström, D. Kressner* A novel parallel QR algorithm for hybrid distributed memory HPC systems
09-14	*M. Gutknecht* IDR explained
09-13	*P. Bientinesi, F.D. Igual, D. Kressner, E.S. Quintana-Orti* Reduction to condensed forms for symmetric eigenvalue problems on multi-core architectures